Amplitude analysis and branching fraction measurement of $D_s^+ \to K^+K^-\pi^+$

M. Ablikim[1], M. N. Achasov[10,c], P. Adlarson[64], S. Ahmed[15], M. Albrecht[4], A. Amoroso[63A,63C], Q. An[60,48], Anita[21], Y. Bai[47], O. Bakina[29], R. Baldini Ferroli[23A], I. Balossino[24A], Y. Ban[38,k], K. Begzsuren[26], J. V. Bennett[5], N. Berger[28], M. Bertani[23A], D. Bettoni[24A], F. Bianchi[63A,63C], J Biernat[64], J. Bloms[57], A. Bortone[63A,63C], I. Boyko[29], R. A. Briere[5], H. Cai[65], X. Cai[1,48], A. Calcaterra[23A], G. F. Cao[1,52], N. Cao[1,52], S. A. Cetin[51B], J. F. Chang[1,48], W. L. Chang[1,52], G. Chelkov[29,b], D. Y. Chen[6], G. Chen[1], H. S. Chen[1,52], M. L. Chen[1,48], S. J. Chen[36], X. R. Chen[25], Y. B. Chen[1,48], W. S. Cheng[63C], G. Cibinetto[24A], F. Cossio[63C], X. F. Cui[37], H. L. Dai[1,48], J. P. Dai[42,g], X. C. Dai[1,52], A. Dbeyssi[15], R. B. de Boer[4], D. Dedovich[29], Z. Y. Deng[1], A. Denig[28], I. Denysenko[29], M. Destefanis[63A,63C], F. De Mori[63A,63C], Y. Ding[34], C. Dong[37], J. Dong[1,48], L. Y. Dong[1,52], M. Y. Dong[1,48,52], S. X. Du[68], J. Fang[1,48], S. S. Fang[1,52], Y. Fang[1], R. Farinelli[24A], L. Fava[63B,63C], F. Feldbauer[4], G. Felici[23A], C. Q. Feng[60,48], M. Fritsch[4], C. D. Fu[1], Y. Fu[1], X. L. Gao[60,48], Y. Gao[38,k], Y. Gao[61], Y. G. Gao[6], I. Garzia[24A,24B], E. M. Gersabeck[55], A. Gilman[56], K. Goetzen[11], L. Gong[37], W. X. Gong[1,48], W. Gradl[28], M. Greco[63A,63C], L. M. Gu[36], M. H. Gu[1,48], S. Gu[2], Y. T. Gu[13], C. Y Guan[1,52], A. Q. Guo[22], L. B. Guo[35], R. P. Guo[40], Y. P. Guo[28], Y. P. Guo[9,h], A. Guskov[29], S. Han[65], T. T. Han[41], T. Z. Han[9,h], X. Q. Hao[16], F. A. Harris[53], K. L. He[1,52], F. H. Heinsius[4], T. Held[4], Y. K. Heng[1,48,52], M. Himmelreich[11,f], T. Holtmann[4], Y. R. Hou[52], Z. L. Hou[1], H. M. Hu[1,52], J. F. Hu[42,g], T. Hu[1,48,52], Y. Hu[1], G. S. Huang[60,48], L. Q. Huang[61], X. T. Huang[41], Z. Huang[38,k], N. Huesken[57], T. Hussain[62], W. Ikegami Andersson[64], W. Imoehl[22], M. Irshad[60,48], S. Jaeger[4], S. Janchiv[26,j], Q. Ji[1], Q. P. Ji[16], X. B. Ji[1,52], X. L. Ji[1,48], H. B. Jiang[41], X. S. Jiang[1,48,52], X. Y. Jiang[37], J. B. Jiao[41], Z. Jiao[18], S. Jin[36], Y. Jin[54], T. Johansson[64], N. Kalantar-Nayestanaki[31], X. S. Kang[34], R. Kappert[31], M. Kavatsyuk[31], B. C. Ke[43,1], I. K. Keshk[4], A. Khoukaz[57], P. Kiese[28], R. Kiuchi[1], R. Kliemt[11], L. Koch[30], O. B. Kolcu[51B,e], B. Kopf[4], M. Kuemmel[4], M. Kuessner[4], A. Kupsc[64], M. G. Kurth[1,52], W. Kühn[30], J. J. Lane[55], J. S. Lange[30], P. Larin[15], L. Lavezzi[63C], H. Leithoff[28], M. Lellmann[28], T. Lenz[28], C. Li[39], C. H. Li[33], Cheng Li[60,48], D. M. Li[68], F. Li[1,48], G. Li[1], H. B. Li[1,52], H. J. Li[9,h], J. L. Li[41], J. Q. Li[4], Ke Li[1], L. K. Li[1], Lei Li[3], P. L. Li[60,48], P. R. Li[32], S. Y. Li[50], W. D. Li[1,52], W. G. Li[1], X. H. Li[60,48], X. L. Li[41], Z. B. Li[49], Z. Y. Li[49], H. Liang[60,48], H. Liang[1,52], Y. F. Liang[45], Y. T. Liang[25], L. Z. Liao[1,52], J. Libby[21], C. X. Lin[49], B. Liu[42,g], B. J. Liu[1], C. X. Liu[1], D. Liu[60,48], D. Y. Liu[42,g], F. H. Liu[44], Fang Liu[1], Feng Liu[6], H. B. Liu[13], H. M. Liu[1,52], Huanhuan Liu[1], Huihui Liu[17], J. B. Liu[60,48], J. Y. Liu[1,52], K. Liu[1], K. Y. Liu[34], Ke Liu[6], L. Liu[60,48], Q. Liu[52], S. B. Liu[60,48], Shuai Liu[46], T. Liu[1,52], X. Liu[32], Y. B. Liu[37], Z. A. Liu[1,48,52], Z. Q. Liu[41], Y. F. Long[38,k], X. C. Lou[1,48,52], F. X. Lu[16], H. J. Lu[18], J. D. Lu[1,52], J. G. Lu[1,48], X. L. Lu[1], Y. Lu[1], Y. P. Lu[1,48], C. L. Luo[35], M. X. Luo[67], P. W. Luo[49], T. Luo[9,h], X. L. Luo[1,48], S. Lusso[63C], X. R. Lyu[52], F. C. Ma[34], H. L. Ma[1], L. L. Ma[41], M. M. Ma[1,52], Q. M. Ma[1], R. Q. Ma[1,52], R. T. Ma[52], X. N. Ma[37], X. X. Ma[1,52], X. Y. Ma[1,48], Y. M. Ma[41], F. E. Maas[15], M. Maggiora[63A,63C], S. Maldaner[28], S. Malde[58], Q. A. Malik[62], A. Mangoni[23B], Y. J. Mao[38,k], Z. P. Mao[1], S. Marcello[63A,63C], Z. X. Meng[54], J. G. Messchendorp[31], G. Mezzadri[24A], T. J. Min[36], R. E. Mitchell[22], X. H. Mo[1,48,52], Y. J. Mo[6], N. Yu. Muchnoi[10,c], H. Muramatsu[56], S. Nakhoul[11,f], Y. Nefedov[29], F. Nerling[11,f], I. B. Nikolaev[10,c], Z. Ning[1,48], S. Nisar[8,i], S. L. Olsen[52], Q. Ouyang[1,48,52], S. Pacetti[23B,23C], X. Pan[46], Y. Pan[55], A. Pathak[1], P. Patteri[23A], M. Pelizaeus[4], H. P. Peng[60,48], K. Peters[11,f], J. Pettersson[64], J. L. Ping[35], R. G. Ping[1,52], A. Pitka[4], R. Poling[56], V. Prasad[60,48], H. Qi[60,48], H. R. Qi[50], M. Qi[36], T. Y. Qi[2], S. Qian[1,48], W.-B. Qian[52], Z. Qian[49], C. F. Qiao[52], L. Q. Qin[12], X. P. Qin[13], X. S. Qin[4], Z. H. Qin[1,48], J. F. Qiu[1], S. Q. Qu[37], K. H. Rashid[62], K. Ravindran[21], C. F. Redmer[28], A. Rivetti[63C], V. Rodin[31], M. Rolo[63C], G. Rong[1,52], Ch. Rosner[15], M. Rump[57], A. Sarantsev[29,d], Y. Schelhaas[28], C. Schnier[4], K. Schoenning[64], D. C. Shan[46], W. Shan[19], X. Y. Shan[60,48], M. Shao[60,48], C. P. Shen[2], P. X. Shen[37], X. Y. Shen[1,52], H. C. Shi[60,48], R. S. Shi[1,52], X. Shi[1,48], X. D Shi[60,48], J. J. Song[41], Q. Q. Song[60,48], W. M. Song[27], Y. X. Song[38,k], S. Sosio[63A,63C], S. Spataro[63A,63C], F. F. Sui[41], G. X. Sun[1], J. F. Sun[16], L. Sun[65], S. S. Sun[1,52], T. Sun[1,52], W. Y. Sun[35], X Sun[20,l], Y. J. Sun[60,48], Y. K Sun[60,48], Y. Z. Sun[1], Z. T. Sun[1], Y. H. Tan[65], Y. X. Tan[60,48], C. J. Tang[45], G. Y. Tang[1], J. Tang[49], V. Thoren[64], B. Tsednee[26], I. Uman[51D], B. Wang[1], B. L. Wang[52], C. W. Wang[36], D. Y. Wang[38,k], H. P. Wang[1,52], K. Wang[1,48], L. L. Wang[1], M. Wang[41], M. Z. Wang[38,k], Meng Wang[1,52], W. H. Wang[65], W. P. Wang[60,48], X. Wang[38,k], X. F. Wang[32], X. L. Wang[9,h], Y. Wang[49], Y. Wang[60,48], Y. D. Wang[15], Y. F. Wang[1,48,52], Y. Q. Wang[1], Z. Wang[1,48], Z. Y. Wang[1], Ziyi Wang[52], Zongyuan Wang[1,52], D. H. Wei[12], P. Weidenkaff[28], F. Weidner[57], S. P. Wen[1], D. J. White[55], U. Wiedner[4], G. Wilkinson[58], M. Wolke[64], L. Wollenberg[4], J. F. Wu[1,52], L. H. Wu[1], L. J. Wu[1,52], X. Wu[9,h], Z. Wu[1,48], L. Xia[60,48], H. Xiao[9,h], S. Y. Xiao[1], Y. J. Xiao[1,52], Z. J. Xiao[35], X. H. Xie[38,k], Y. G. Xie[1,48], Y. H. Xie[6], T. Y. Xing[1,52], X. A. Xiong[1,52], G. F. Xu[1], J. J. Xu[36], Q. J. Xu[14], W. Xu[1,52], X. P. Xu[46], L. Yan[63A,63C], L. Yan[9,h], W. B. Yan[60,48], W. C. Yan[68], Xu Yan[46], H. J. Yang[42,g], H. X. Yang[1], L. Yang[65],

R. X. Yang[60,48], S. L. Yang[1,52], Y. H. Yang[36], Y. X. Yang[12], Yifan Yang[1,52], Zhi Yang[25], M. Ye[1,48], M. H. Ye[7], J. H. Yin[1], Z. Y. You[49], B. X. Yu[1,48,52], C. X. Yu[37], G. Yu[1,52], J. S. Yu[20,l], T. Yu[61], C. Z. Yuan[1,52], W. Yuan[63A,63C], X. Q. Yuan[38,k], Y. Yuan[1], Z. Y. Yuan[49], C. X. Yue[33], A. Yuncu[51B,a], A. A. Zafar[62], Y. Zeng[20,l], B. X. Zhang[1], Guangyi Zhang[16], H. H. Zhang[49], H. Y. Zhang[1,48], J. L. Zhang[66], J. Q. Zhang[4], J. W. Zhang[1,48,52], J. Y. Zhang[1], J. Z. Zhang[1,52], Jianyu Zhang[1,52], Jiawei Zhang[1,52], L. Zhang[1], Lei Zhang[36], S. Zhang[49], S. F. Zhang[36], T. J. Zhang[42,g], X. Y. Zhang[41], Y. Zhang[58], Y. H. Zhang[1,48], Y. T. Zhang[60,48], Yan Zhang[60,48], Yao Zhang[1], Yi Zhang[9,h], Z. H. Zhang[6], Z. Y. Zhang[65], G. Zhao[1], J. Zhao[33], J. Y. Zhao[1,52], J. Z. Zhao[1,48], Lei Zhao[60,48], Ling Zhao[1], M. G. Zhao[37], Q. Zhao[1], S. J. Zhao[68], Y. B. Zhao[1,48], Y. X. Zhao[25], Z. G. Zhao[60,48], A. Zhemchugov[29,b], B. Zheng[61], J. P. Zheng[1,48], Y. Zheng[38,k], Y. H. Zheng[52], B. Zhong[35], C. Zhong[61], L. P. Zhou[1,52], Q. Zhou[1,52], X. Zhou[65], X. K. Zhou[52], X. R. Zhou[60,48], A. N. Zhu[1,52], J. Zhu[37], K. Zhu[1], K. J. Zhu[1,48,52], S. H. Zhu[59], W. J. Zhu[37], X. L. Zhu[50], Y. C. Zhu[60,48], Z. A. Zhu[1,52], B. S. Zou[1], J. H. Zou[1]

(BESIII Collaboration)

[1] *Institute of High Energy Physics, Beijing 100049, People's Republic of China*
[2] *Beihang University, Beijing 100191, People's Republic of China*
[3] *Beijing Institute of Petrochemical Technology, Beijing 102617, People's Republic of China*
[4] *Bochum Ruhr-University, D-44780 Bochum, Germany*
[5] *Carnegie Mellon University, Pittsburgh, Pennsylvania 15213, USA*
[6] *Central China Normal University, Wuhan 430079, People's Republic of China*
[7] *China Center of Advanced Science and Technology, Beijing 100190, People's Republic of China*
[8] *COMSATS University Islamabad, Lahore Campus, Defence Road, Off Raiwind Road, 54000 Lahore, Pakistan*
[9] *Fudan University, Shanghai 200443, People's Republic of China*
[10] *G.I. Budker Institute of Nuclear Physics SB RAS (BINP), Novosibirsk 630090, Russia*
[11] *GSI Helmholtzcentre for Heavy Ion Research GmbH, D-64291 Darmstadt, Germany*
[12] *Guangxi Normal University, Guilin 541004, People's Republic of China*
[13] *Guangxi University, Nanning 530004, People's Republic of China*
[14] *Hangzhou Normal University, Hangzhou 310036, People's Republic of China*
[15] *Helmholtz Institute Mainz, Johann-Joachim-Becher-Weg 45, D-55099 Mainz, Germany*
[16] *Henan Normal University, Xinxiang 453007, People's Republic of China*
[17] *Henan University of Science and Technology, Luoyang 471003, People's Republic of China*
[18] *Huangshan College, Huangshan 245000, People's Republic of China*
[19] *Hunan Normal University, Changsha 410081, People's Republic of China*
[20] *Hunan University, Changsha 410082, People's Republic of China*
[21] *Indian Institute of Technology Madras, Chennai 600036, India*
[22] *Indiana University, Bloomington, Indiana 47405, USA*
[23] *(A)INFN Laboratori Nazionali di Frascati, I-00044, Frascati, Italy; (B)INFN Sezione di Perugia, I-06100, Perugia, Italy; (C)University of Perugia, I-06100, Perugia, Italy*
[24] *(A)INFN Sezione di Ferrara, I-44122, Ferrara, Italy; (B)University of Ferrara, I-44122, Ferrara, Italy*
[25] *Institute of Modern Physics, Lanzhou 730000, People's Republic of China*
[26] *Institute of Physics and Technology, Peace Ave. 54B, Ulaanbaatar 13330, Mongolia*
[27] *Jilin University, Changchun 130012, People's Republic of China*
[28] *Johannes Gutenberg University of Mainz, Johann-Joachim-Becher-Weg 45, D-55099 Mainz, Germany*
[29] *Joint Institute for Nuclear Research, 141980 Dubna, Moscow region, Russia*
[30] *Justus-Liebig-Universitaet Giessen, II. Physikalisches Institut, Heinrich-Buff-Ring 16, D-35392 Giessen, Germany*
[31] *KVI-CART, University of Groningen, NL-9747 AA Groningen, The Netherlands*
[32] *Lanzhou University, Lanzhou 730000, People's Republic of China*
[33] *Liaoning Normal University, Dalian 116029, People's Republic of China*
[34] *Liaoning University, Shenyang 110036, People's Republic of China*
[35] *Nanjing Normal University, Nanjing 210023, People's Republic of China*
[36] *Nanjing University, Nanjing 210093, People's Republic of China*
[37] *Nankai University, Tianjin 300071, People's Republic of China*
[38] *Peking University, Beijing 100871, People's Republic of China*
[39] *Qufu Normal University, Qufu 273165, People's Republic of China*

[40] *Shandong Normal University, Jinan 250014, People's Republic of China*
[41] *Shandong University, Jinan 250100, People's Republic of China*
[42] *Shanghai Jiao Tong University, Shanghai 200240, People's Republic of China*
[43] *Shanxi Normal University, Linfen 041004, People's Republic of China*
[44] *Shanxi University, Taiyuan 030006, People's Republic of China*
[45] *Sichuan University, Chengdu 610064, People's Republic of China*
[46] *Soochow University, Suzhou 215006, People's Republic of China*
[47] *Southeast University, Nanjing 211100, People's Republic of China*
[48] *State Key Laboratory of Particle Detection and Electronics, Beijing 100049, Hefei 230026, People's Republic of China*
[49] *Sun Yat-Sen University, Guangzhou 510275, People's Republic of China*
[50] *Tsinghua University, Beijing 100084, People's Republic of China*
[51] *(A)Ankara University, 06100 Tandogan, Ankara, Turkey; (B)Istanbul Bilgi University, 34060 Eyup, Istanbul, Turkey; (C)Uludag University, 16059 Bursa, Turkey; (D)Near East University, Nicosia, North Cyprus, Mersin 10, Turkey*
[52] *University of Chinese Academy of Sciences, Beijing 100049, People's Republic of China*
[53] *University of Hawaii, Honolulu, Hawaii 96822, USA*
[54] *University of Jinan, Jinan 250022, People's Republic of China*
[55] *University of Manchester, Oxford Road, Manchester, M13 9PL, United Kingdom*
[56] *University of Minnesota, Minneapolis, Minnesota 55455, USA*
[57] *University of Muenster, Wilhelm-Klemm-Str. 9, 48149 Muenster, Germany*
[58] *University of Oxford, Keble Rd, Oxford, UK OX13RH*
[59] *University of Science and Technology Liaoning, Anshan 114051, People's Republic of China*
[60] *University of Science and Technology of China, Hefei 230026, People's Republic of China*
[61] *University of South China, Hengyang 421001, People's Republic of China*
[62] *University of the Punjab, Lahore-54590, Pakistan*
[63] *(A)University of Turin, I-10125, Turin, Italy; (B)University of Eastern Piedmont, I-15121, Alessandria, Italy; (C)INFN, I-10125, Turin, Italy*
[64] *Uppsala University, Box 516, SE-75120 Uppsala, Sweden*
[65] *Wuhan University, Wuhan 430072, People's Republic of China*
[66] *Xinyang Normal University, Xinyang 464000, People's Republic of China*
[67] *Zhejiang University, Hangzhou 310027, People's Republic of China*
[68] *Zhengzhou University, Zhengzhou 450001, People's Republic of China*

[a] *Also at Bogazici University, 34342 Istanbul, Turkey*
[b] *Also at the Moscow Institute of Physics and Technology, Moscow 141700, Russia*
[c] *Also at the Novosibirsk State University, Novosibirsk, 630090, Russia*
[d] *Also at the NRC "Kurchatov Institute", PNPI, 188300, Gatchina, Russia*
[e] *Also at Istanbul Arel University, 34295 Istanbul, Turkey*
[f] *Also at Goethe University Frankfurt, 60323 Frankfurt am Main, Germany*
[g] *Also at Key Laboratory for Particle Physics, Astrophysics and Cosmology, Ministry of Education; Shanghai Key Laboratory for Particle Physics and Cosmology; Institute of Nuclear and Particle Physics, Shanghai 200240, People's Republic of China*
[h] *Also at Key Laboratory of Nuclear Physics and Ion-beam Application (MOE) and Institute of Modern Physics, Fudan University, Shanghai 200443, People's Republic of China*
[i] *Also at Harvard University, Department of Physics, Cambridge, MA, 02138, USA*
[j] *Currently at: Institute of Physics and Technology, Peace Ave.54B, Ulaanbaatar 13330, Mongolia*
[k] *Also at State Key Laboratory of Nuclear Physics and Technology, Peking University, Beijing 100871, People's Republic of China*
[l] *School of Physics and Electronics, Hunan University, Changsha 410082, China*

(Dated: October 20, 2022)

We report an amplitude analysis and branching fraction measurement of $D_s^+ \to K^+K^-\pi^+$ decay using a data sample of 3.19 fb^{-1} recorded with BESIII detector at a center-of-mass energy of 4.178 GeV. We perform a model-independent partial wave analysis in the low K^+K^- mass region to determine the K^+K^- S-wave lineshape, followed by an amplitude analysis of our very pure high-statistics sample. The amplitude analysis provides an accurate determination of the detection efficiency allowing us to measure the branching fraction $\mathcal{B}(D_s^+ \to K^+K^-\pi^+) = (5.47 \pm 0.08_{\rm stat} \pm 0.13_{\rm sys})\%$.

PACS numbers: 13.20.Fc, 12.38.Qk, 14.40.Lb

I. INTRODUCTION

The decay $D_s^+ \to K^+K^-\pi^+$ is widely used as a reference mode in $D_s^\pm$ analyses because of its large branching fraction (BF) and low background contamination. An amplitude analysis can reveal the intermediate states involved in this decay and thereby reduce the detection efficiency systematic uncertainties. The improved precision of the BF is important for $D_s^\pm$ analysis using this decay as a reference channel. Furthermore, theoretical studies [1] predict the BFs of $D_s^+ \to \bar{K}^*(892)^0K^+$ and $D_s^+ \to \phi(1020)\pi^+$ to be in the range of $(3.9-4.2)\%$ and $(3.4-4.51)\%$, respectively. Combining the results of the amplitude analysis and the BF measurement, one can obtain the BFs of such intermediate processes, which can help to improve the theoretical model [1].

Dalitz plot analyses of the $D_s^+ \to K^+K^-\pi^+$ decay have been performed by the E687 [2], CLEO [3] and BaBar [4] collaborations. The E687 collaboration used about 700 pure signal events and did not take the $f_0(1370)\pi^+$ intermediate state into account. In the CLEO analysis about 14400 events with a purity of 84.9% were selected in an untagged analysis of 0.586 fb^{-1} of data similar to the present analysis. The analysis of BaBar collaboration used about 100 000 events with a purity of about 95%. Table I shows the comparison of the fit fractions (FFs) from these previous Dalitz plot analyses. There are obvious differences between FFs of BaBar collaboration and CLEO collaboration.

The decay $D_s^+ \to a_0(980)^0\pi^+$ has been observed through $D_s^+ \to \pi^+\pi^0\eta$ [5], and should also be present in $D_s^+ \to K^+K^-\pi^+$, which was not taken into account before. Due to the strong overlap of $a_0(980) \to K^+K^-$ and $f_0(980) \to K^+K^-$ and their common J^{PC}, we do not distinguish between them in this paper and denote the combined state as $S(980)$. A model-independent partial wave analysis (MIPWA) is performed to study this low-mass resonance.

In this paper we report an amplitude analysis and BF measurement of $D_s^+ \to K^+K^-\pi^+$ (the inclusion of charge conjugates is implied) using a 3.19 fb^{-1} data sample collected with the BESIII detector at a center-of-mass energy ($E_{\rm CMS}$) of 4.178 GeV. At this energy, the cross section for the $D_s^{*\pm}D_s^\mp$ final state in e^+e^- annihilations is one order magnitude larger than that for $D_s^+D_s^-$ [6]. Moreover, the $D_s^{*\pm}$ decays are dominated by the process $D_s^{*\pm} \to \gamma D_s^\pm$ [7]. Thus, the process $e^+e^- \to D_s^{*\pm}D_s^\mp \to D_s^+\gamma D_s^-$ is the main signal process. Using a tagging technique [8] (described in Sec. IV A), we get a nearly background-free data sample to use for an amplitude analysis and BF measurement. The process $e^+e^- \to D_s^+D_s^-$ also contributes to the BF measurement. For the amplitude analysis (Sec. IV) and BF measurement (Sec. V), both the signal D_s and the other D_s are reconstructed, while for the MIPWA (Sec. A) only the signal decay is reconstructed.

II. BESIII DETECTOR AND DATA SETS

The BESIII detector is a magnetic spectrometer [9] located at the Beijing Electron Positron Collider (BEPCII) [10]. The inner subdetectors are surrounded by a superconducting solenoidal magnet which provide a 1.0 T magnetic field. Starting from the interaction point these consist of a main drift chamber (MDC), a plastic scintillator time-of-flight (TOF) system, a CsI(Tl) electromagnetic calorimeter (EMC). Charged particle identification is performed by combining the ionization energy loss (dE/dx) measured by the MDC and the time-of-flight measured by the TOF. The EMC provides shower information to reconstruct photons. Outside the solenoidal magnet is a multi-gap resistive-plate chamber system, which provides muon identification.

Monte Carlo (MC) samples are produced with GEANT4-based [11] software. An inclusive MC sample is produced at $E_{\rm CMS} = 4.178$ GeV. The sample includes all known open charm production processes, the continuum processes ($e^+e^- \to q\bar{q}$, $q = u, d$ and s), Bhabha scattering, $\mu^+\mu^-$, $\tau^+\tau^-$, diphoton process and production of the $c\bar{c}$ resonances J/ψ, $\psi(3686)$ and $\psi(3770)$ via initial state radiation (ISR). The generator CONEXC [12] is used to model the open charm processes directly produced via e^+e^- annihilation. The simulation of ISR production of $\psi(3770)$, $\psi(3686)$ and J/ψ is performed with the KKMC [13]. The known decays with BFs taken from the Particle Data Group (PDG) [7] are simulated with the EVENTGEN [14] and the unknown decays are generated with the LUNDCHARM model [15]. Final-state radiation from charged tracks is produced by the PHOTOS [16]. The signal selection efficiency is obtained from MC samples of $e^+e^- \to D_s^{(*)}D_s$, in which the D_s^+ meson decays into $K^+K^-\pi^+$ while the D_s^- meson decays to one of the tag modes listed in Table II. Two such samples

TABLE I. Comparison of FFs for different decay modes. The first and second uncertainties are statistical and systematic, respectively.

Decay mode	FF(%)		
	E687	CLEO	BaBar
$D_s^+ \to \bar{K}^*(892)^0 K^+$	47.8±4.6±4.0	47.4±1.5±0.4	47.9±0.5±0.5
$D_s^+ \to \phi(1020)\pi^+$	39.6±3.3±4.7	42.2±1.6±0.3	41.4±0.8±0.5
$D_s^+ \to f_0(980)\pi^+$	11.0±3.5±2.6	28.2±1.9±1.8	16.4±0.7±2.0
$D_s^+ \to \bar{K}_0^*(1430)^0 K^+$	9.3±3.2±3.2	3.9±0.5±0.5	2.4±0.3±1.0
$D_s^+ \to f_0(1710)\pi^+$	3.4±2.3±3.5	3.4±0.5±0.3	1.1±0.1±0.1
$D_s^+ \to f_0(1370)\pi^+$		4.3±0.6±0.5	1.1±0.1±0.2
$\sum$FF(%)	111.1	129.5±4.4±2.0	110.2±0.6±2.0
Events	701±36	12226±122	96307±369

are generated. The one with a uniform distribution of $D_s^+ \to K^+K^-\pi^+$ decays over the phase space (PHSP) is called "PHSP MC". In the second sample, called "signal MC", the $D_s^+ \to K^+K^-\pi^+$ decay is generated according to the model obtained from the amplitude analysis presented in this paper.

III. EVENT SELECTION

The polar angles (θ) of charged tracks with respect to the beam axis must satisfy $|\cos\theta| < 0.93$. Except for tracks from K_S^0 decays, the distances of closest approach to the beamspot for charged tracks in the transverse plane and along the beam direction must be less than 1 cm and 10 cm, respectively.

Photons are reconstructed from showers in the EMC. The deposited energies of the photons from the endcap ($0.86 < |\cos\theta| < 0.92$) should be larger than 50 MeV and those of the photons from the barrel ($|\cos\theta| < 0.80$) should be larger than 25 MeV. Furthermore, the shower should be detected within 700 ns after a beam crossing.

Candidates for $\pi^0(\eta)$ decay are reconstructed through $\pi^0 \to \gamma\gamma$ ($\eta \to \gamma\gamma$). The diphoton invariant mass $M_{\gamma\gamma}$ for π^0 (η) should be in the range of $0.115 < M_{\gamma\gamma} < 0.150$ GeV/c^2 ($0.490 < M_{\gamma\gamma} < 0.580$ GeV/c^2). A 1C kinematic fit constraining $M_{\gamma\gamma}$ to the π^0 or η nominal mass [7] is performed, and the χ^2 of the corresponding fit should be less than 30 for π^0 or η candidates.

Kaons and pions are identified by combining the dE/dx information in the MDC and the time-of-flight from the TOF. If the probability of the kaon hypothesis is larger than that of the pion hypothesis, the track is identified as a kaon. Otherwise, the track is identified as a pion. Any $\pi^\pm$ and π^0 candidates with momentum less than 0.1 GeV/c are vetoed to remove soft $\pi^\pm$ and π^0 from D^* decays.

Pairs of $\pi^+\pi^-$ are used to reconstruct K_S^0 mesons. The polar angles θ of the two pions should satisfy $|\cos\theta| < 0.93$. The distances of closest approach to the beamspot along the beam direction should be less than 20 cm. The invariant mass $m(\pi^+\pi^-)$ of $\pi^+\pi^-$ pairs should satisfy $0.487 < m(\pi^+\pi^-) < 0.511$ GeV/c^2. A secondary vertex fit, constraining the pion candidate pair to a common vertex is performed to determine the decay length L of the K_S. We require $L/\sigma_L > 2$, where σ_L is the uncertainty on L.

The η' candidates are reconstructed via the process $\eta' \to \pi^+\pi^-\eta$. Candidates with a $\pi^+\pi^-\eta$ invariant mass in the range of $[0.938, 0.978]$ GeV/c^2 are retained.

Tagged D_s candidates are reconstructed from various combinations of $K^\pm$, $\pi^\pm$, η, η', K_S^0 and π^0, while the signal D_s^+ candidates are reconstructed from $K^+K^-\pi^+$ combinations. Candidates with an invariant mass in the mass window $[1.87, 2.06]$ GeV/c^2 and a recoiling mass $M_{\rm rec}$ in the mass window $[2.051, 2.180]$ GeV/c^2 are retained. The recoiling mass $M_{\rm rec}$ is defined as:

$$M_{\rm rec} = \sqrt{(E_{\rm CMS} - \sqrt{|\,\vec{p}_{D_s}\,|^2 + m_{D_s}^2})^2 - |\,\vec{p}_{D_s}\,|^2}\,, \quad (1)$$

where $\vec{p}_{D_s}$ is the momentum of D_s candidate in e^+e^- center-of-mass system, m_{D_s} is D_s mass quoted from PDG [7]. The requirement on $M_{\rm rec}$ is chosen to retain both the monochromatic D_s that are produced directly from the e^+e^- collision as well as the broader distribution that arises from $D_s^{*\pm} \to D_s^\pm\gamma$ decays.

IV. AMPLITUDE ANALYSIS

An unbinned maximum likelihood method is used to determine the intermediate resonance composition in the decay $D_s^+ \to K^+K^-\pi^+$. The likelihood function is constructed with a probability density function (PDF) which depends on the momenta of the three daughter particles.

A. Tag Technique in Amplitude Analysis

As D_s mesons are produced in pairs, D_s mesons can be reconstructed with a tag technique which provides both single tag (ST) and double tag (DT) samples. In the ST samples, only one D_s^- meson is reconstructed through selected hadronic D_s decays, the so-called tag modes. The eight tag modes used in the amplitude analysis and BF measurement presented in Sec. V are $D_s^- \to K^+K^-\pi^-$, $K_S^0K^-$, $K_S^0K^-\pi^+\pi^-$, $K^-\pi^+\pi^-$, $K_S^0K^+\pi^-\pi^-$, $\pi^+\pi^-\pi^-$, $\pi^-\eta'_{\pi^+\pi^-\eta_{\gamma\gamma}}$ and $K^+K^-\pi^-\pi^0$, here, $\eta'_{\pi^+\pi^-\eta_{\gamma\gamma}}$ denotes $\eta' \to \pi^+\pi^-\eta$ with $\eta \to \gamma\gamma$. In the DT samples, photons from the decay $D_s^{*\pm} \to D_s^{\pm}\gamma$, tag mode D_s^- and signal D_s^+ (i.e., decays to $K^+K^-\pi^+$) are all fully reconstructed. A five-constraint (5C) kinematic fit is performed, constraining the four-momentum of the $D_s^{*\pm}D_s^{\mp}$ system to the initial four-momentum of the electron-positron system and the invariant mass of the $D_s^{*\pm}$ to the corresponding PDG value [7]. For each $D_s^+D_s^-\gamma$ candidate, the extra γ is paired with both the tag and signal D_s to form the $D_s^{*\pm}$, and the combination with the lower fit $\chi^2_{\rm 5C}$ is retained as the presumably correct pairing. If there are multiple candidate $D_s^{*\pm}D_s^{\mp}$ pairs in an event, the candidate with minimum $\chi^2_{\rm 5C}$ is selected as the best one. The invariant mass of signal D_s ($m_{\rm sig}$) and tag D_s ($m_{\rm tag}$) candidates are required to be within the mass regions shown in Table II.

TABLE II. The mass windows for the signal mode and various tag modes.

Mode	Mass window (GeV/c^2)
$D_s^- \to K_S^0K^-$	[1.948, 1.991]
$D_s^{\pm} \to K^{\pm}K^{\mp}\pi^{\pm}$	[1.950, 1.986]
$D_s^- \to K^+K^-\pi^-\pi^0$	[1.947, 1.982]
$D_s^- \to K_S^0K^-\pi^+\pi^-$	[1.958, 1.980]
$D_s^- \to K_S^0K^+\pi^-\pi^-$	[1.953, 1.983]
$D_s^- \to \pi^-\pi^-\pi^+$	[1.952, 1.984]
$D_s^- \to \pi^-\eta'_{\pi^+\pi^-\eta_{\gamma\gamma}}$	[1.940, 1.996]
$D_s^- \to K^-\pi^+\pi^-$	[1.953, 1.983]

To ensure that all events fall within the physical region on the Dalitz plot, we perform a 7C fit where constraints on both signal and tag D_s masses to the PDG values are added to the previous 5C constraints. The four-momenta of the tracks after 7C fit are used to perform the amplitude analysis.

The background of the DT sample in the amplitude analysis is estimated using the inclusive MC sample. The fit to the signal D_s invariant mass without 7C kinematic fit gives the signal yield and purity, as shown in Fig. 1. In the fit, the signal shape is modeled with the MC-simulated shape convolved with a Gaussian function while the background is described with a second-order Chebychev polynomial. There is no obvious peaking background in the signal region ($1.950 < m_{\rm sig} < 1.986$ GeV/c^2) and we obtain 4399 signal candidates with a purity of 99.6%. Figure 2 shows the Dalitz plot of the signal $D_s^+ \to K^+K^-\pi^+$ candidates.

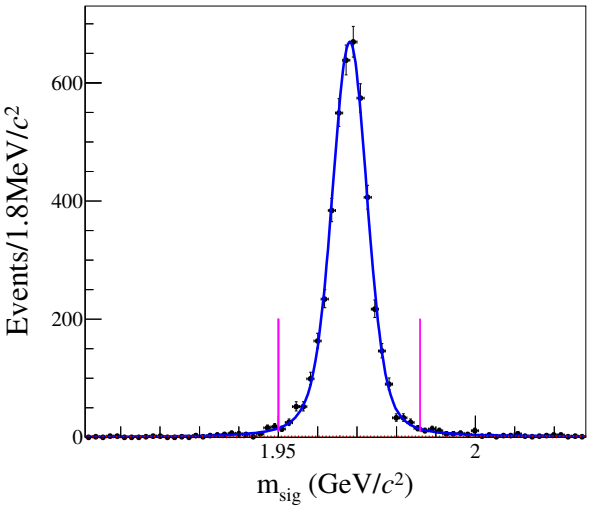

FIG. 1. The fit to the signal D_s invariant mass $m_{\rm sig}$ before the 7C kinematic fit (dots with error bars). The area between the pink lines is the signal area of the sample for the amplitude analysis.

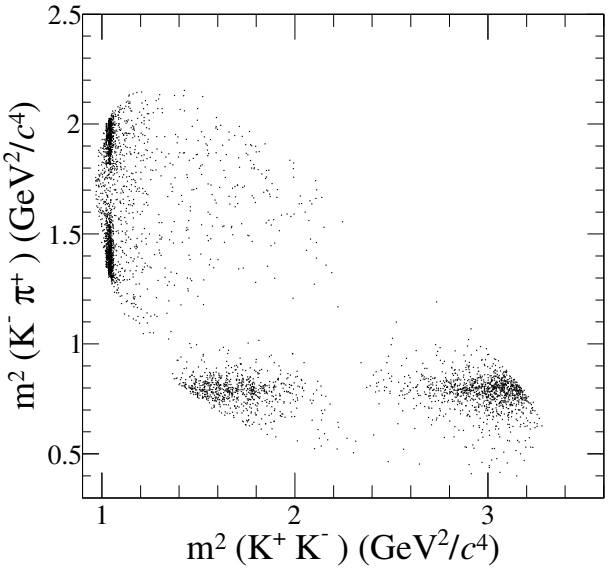

FIG. 2. The Dalitz plot of selected $D_s^+ \to K^+K^-\pi^+$ candidates.

B. Likelihood Function Construction

For a three-body process the amplitude $A_n(p)$ for the $n^{\rm th}$ mode may be written as

$$A_n(p) = P_n(p)S_n(p)F_n^r(p)F_n^D(p), \tag{2}$$

where p refers to the set of the three daughter particles' four-momenta, $P_n(p)$ is the propagator, $S_n(p)$ is the spin factor constructed with the covariant tensor formalism [17], $F_n^r(p)$ and $F_n^D(p)$ are the Blatt-Weisskopf barrier factors for the intermediate resonance and D_s meson decays, respectively. According to the isobar formulation, the total amplitude $M(p)$ is obtained by the coherent sum of all intermediate modes:

$$M(p) = \sum c_n A_n(p), \tag{3}$$

where $c_n = \rho_n e^{i\phi}$ is the complex coefficient of the $n^{\rm th}$ mode, ρ_n and ϕ_n are the magnitude and phase of c_n, respectively. Then the signal PDF $f_S(p)$ is given by:

$$f_S(p) = \frac{\epsilon(p)\left|M(p)\right|^2 R_3(p)}{\int \epsilon(p)\left|M(p)\right|^2 R_3(p)\,dp}, \tag{4}$$

where $\epsilon(p)$ is the detection efficiency and $R_3(p)$ is the three-particle phase space, which is defined as:

$$R_3(p)dp = (2\pi)^4\,\delta^4\left(p_{D_s} - \sum_{\alpha=1}^{3} p_\alpha\right)\prod_{\alpha=1}^{3}\frac{d^3p_\alpha}{(2\pi)^3 2E_\alpha}, \tag{5}$$

where $\alpha = 1,2,3$ is the index of the three daughter particles. The likelihood function is given by

$$\begin{aligned}\ln\mathcal{L} &= \sum_{k}^{N_{\rm data}} \ln f_S(p^k) \\ &= \sum_{k}^{N_{\rm data}} \ln\left(\frac{\left|M(p)\right|^2}{\int \epsilon(p)\left|M(p)\right|^2 R_3(p)\,dp}\right) \\ &+ \sum_{k}^{N_{\rm data}} \ln\left(R_3(p)\epsilon(p)\right),\end{aligned} \tag{6}$$

where $N_{\rm data}$ is the number of candidate events in data. Background contribution is neglected in the amplitude analysis and the possible bias is included to the systematic uncertainties, see Sec. IV D below. The normalization integral in Eq. (6) is first determined by the following equation using PHSP MC events with a uniform distribution:

$$\begin{aligned}&\int \epsilon(p)\left|M(p)\right|^2 R_3(p)\,dp \\ &\approx \frac{1}{N_{\rm MC,gen}}\sum_{k_{\rm MC}}^{N_{\rm MC,sel}}\left|M(p^{k_{\rm MC}})\right|^2,\end{aligned} \tag{7}$$

where $p^{k_{\rm MC}}$ is the $k_{\rm MC}^{\rm th}$ set of four-momenta. Here, $N_{\rm MC,gen}$ and $N_{\rm MC,sel}$ are the numbers of generated phase-space events and selected phase-space events, respectively. A set of estimated c_n can be obtained from a preliminary fit using the phase-space MC to evaluate the normalization integral. Assuming the estimated values to be c_n', the normalization integral can be evaluated with signal MC samples:

$$\begin{aligned}&\int \epsilon(p)\left|M(p)\right|^2 R_3(p)\,dp \\ &\approx \frac{1}{N_{\rm MC}}\sum_{k_{\rm MC}}^{N_{\rm MC}}\frac{\left|M(p^{k_{\rm MC}})\right|^2}{\left|M^{\rm gen}(p^{k_{\rm MC}})\right|^2},\end{aligned} \tag{8}$$

where $M^{\rm gen}(p^{k_{\rm MC}})$ is the PDF modeled with c_n' to generate signal MC and $N_{\rm MC}$ is the number of events in the MC sample. The computational efficiency of the MC integration is significantly improved by evaluating the normalization integral with signal MC samples, which intrinsically take into account the event selection acceptance and the detection resolution. Correction factors γ_ϵ are introduced to correct for the bias caused by PID and tracking efficiency inconsistencies between data and MC simulation:

$$\gamma_\epsilon = \prod_j \frac{\epsilon_{j,data}(p)}{\epsilon_{j,MC}(p)}, \tag{9}$$

where j refers to PID or tracking, $\epsilon_{j,data}$ and $\epsilon_{j,MC}$ refer to the PID or tracking efficiencies for data and MC, respectively. Taking the correction factors γ_ϵ into account, the normalization integral can be obtained by:

$$\begin{aligned}&\int \epsilon(p)\left|M(p)\right|^2 R_3(p)\,dp \\ &\approx \frac{1}{N_{\rm MC}}\sum_{k_{\rm MC}}^{N_{\rm MC}}\frac{\left|M(p^{k_{\rm MC}})\right|^2\gamma_\epsilon}{\left|M^{\rm gen}(p^{k_{\rm MC}})\right|^2}.\end{aligned} \tag{10}$$

1. *Propagator and Blatt-Weisskopf Barrier*

For a given two-body decay ($a \to bc$), p_a, p_b and p_c are the momenta of particles a, b and c. The variables s_a, s_b and s_c refer to the squared invariant masses of particles a, b and c. The momentum q is defined as the magnitude of the momentum of b or c in the rest system of a:

$$q = \sqrt{\frac{(s_a + s_b - s_c)^2}{4s_a} - s_b}. \tag{11}$$

The resonances $K^*(892)$, $f_0(1710)$, $\phi(1020)$ and $f_0(1370)$ are parameterized with a relativistic Breit-Wigner formula,

$$\begin{aligned}P &= \tfrac{1}{(m_0^2 - s_a) - im_0\Gamma(m)}, \\ \Gamma(m) &= \Gamma_0\left(\tfrac{q}{q_0}\right)^{2L+1}\left(\tfrac{m_0}{m}\right)\left(\tfrac{F_L(q)}{F_L(q_0)}\right)^2,\end{aligned} \tag{12}$$

where m_0 and Γ_0 are the mass and the width of the intermediate resonance, fixed to the PDG values [7], with the exception of $f_0(1370)$. The mass and width of $f_0(1370)$ are fixed to 1350 MeV/c^2 and 265 MeV [18], respectively. The value of q_0 in Eq. (12) is that of q when $s_a = m_0^2$, L denotes the angular momenta and Blatt-Weisskopf Barrier $F_L(q)$ is defined as:

$$\begin{aligned} F_{L=0}(q) &= 1, \\ F_{L=1}(q) &= \sqrt{\tfrac{2z^2}{z^2+1}}, \\ F_{L=2}(q) &= \sqrt{\tfrac{13z^4}{9z^4+3z^2+1}}, \end{aligned} \tag{13}$$

where $z = qR$. R is the effective radius of the intermediate resonance or D_s meson. The values of R are fixed to 3.0 GeV^{-1} for intermediate states and 5.0 GeV^{-1} for D_s meson, respectively. The ambiguity of R values is taken into account in evaluation of the systematic uncertainties.

The $K_0^*(1430)^0$ is parameterized with the Flatté formula:

$$P_{K_0^*(1430)^0} = \frac{1}{M^2 - s - i(g_1\rho_{K\pi}(s) + g_2\rho_{\eta' K}(s))}, \tag{14}$$

where s is the squared $K^-\pi^+$ invariant mass, $\rho_{K\pi}(s)$ and $\rho_{\eta' K}(s)$ are Lorentz invariant PHSP factor, and $g_{1,2}$ are coupling constants to the corresponding final state. The parameters of the $K_0^*(1430)^0$ are fixed to values measured by CLEO [19].

For the resonance $S(980)$ (representing the $f_0(980)$ and $a_0(980)$), we use Eq. (A6) in the appendix to describe the propagator and the values of parameters are fixed to those in Eq. (A7) obtained from the model-independent partial wave analysis section (Sec. A).

2. Spin Factors

The spin projection operators [17] for a two-body decay are defined as

$$\begin{aligned} P^0(a) &= 1, \\ P^{(1)}_{\mu\mu'}(a) &= -g_{\mu\mu'} + \frac{p_{a,\mu}p_{a,\mu'}}{p_a^2}, \\ P^{(2)}_{\mu\nu\mu'\nu'}(a) &= \frac{1}{2}(P^{(1)}_{\mu\mu'}(a)P^{(1)}_{\nu\nu'}(a) + P^{(1)}_{\mu\nu'}(a)P^{(1)}_{\nu\mu'}(a)) \\ &\quad - \frac{1}{3}P^{(1)}_{\mu\nu}(a)P^{(1)}_{\mu'\nu'}(a). \end{aligned} \tag{15}$$

The corresponding covariant tensors are expressed as follows

$$\begin{aligned} \tilde{t}^{(0)}(a) &= 1, \\ \tilde{t}^{(1)}_{\mu}(a) &= -P^{(1)}_{\mu\mu'}(a)r_a^{\mu'}, \\ \tilde{t}^{(2)}_{\mu\nu}(a) &= P^{(2)}_{\mu\nu\mu'\nu'}(a)r_a^{\mu'}r_a^{\nu'}, \end{aligned} \tag{16}$$

where $r_a = p_b - p_c$ is the momentum difference between b and c. The spin factor for the process $D_s \to aX$ (where a is a resonance and X is a direct daughter of the D_s meson) with $a \to bc$ is,

$$\begin{aligned} S_n &= 1, \\ S_n &= \tilde{T}^{(1)\mu}(D_s)\tilde{t}^{(1)}_{\mu}(a), \\ S_n &= \tilde{T}^{(2)\mu\nu}(D_s)\tilde{t}^{(2)}_{\mu\nu}(a), \end{aligned} \tag{17}$$

where $\tilde{T}^{(L)}_{\mu}(D_s)$ and $\tilde{t}^{(L)}_{\mu}(a)$ are the covariant tensors with angular momenta L for $D_s \to aX$ and $a \to bc$, respectively.

C. Fit Result

Clear peaks for both $\bar{K}^*(892)^0$ and $\phi(1020)$ can be seen in Fig. 2. We choose $\bar{K}^*(892)^0$ as the reference amplitude and fix the magnitude ρ and phase ϕ for $D_s^+ \to \bar{K}^*(892)^0K^+$ to 1.0 and 0.0, respectively. The magnitudes and phases of other processes are free parameters in the fit. Possible processes are retained in the fit according to their statistical significances. We calculate the statistical significance for a certain intermediate process using the change of likelihood and number of degrees of freedom. Processes with significances less than 5σ are discarded. The six intermediate processes retained in the nominal fit are $D_s^+ \to \bar{K}^*(892)^0K^+$, $\phi(1020)\pi^+$, $S(980)\pi^+$, $\bar{K}_0^*(1430)^0K^+$, $f_0(1370)\pi^+$ and $f_0(1710)\pi^+$. The magnitudes, phases and corresponding significances of these amplitudes are listed in Table III. The systematic uncertainties are discussed in Sec. IV D.

With the coefficients c_n obtained from the fit, the FFs are calculated with generator-level phase-space MC as

$$\mathrm{FF}(n) = \frac{\sum |c_n A_n|^2}{\sum |M(p_j^k)|^2}, \tag{18}$$

where the summation is performed over the generated PHSP MC events.

To properly treat correlations, we randomly vary the coefficients c_n according to the corresponding error matrix to produce many sets of c_n and then obtain a series of FFs for each intermediate process. A Gaussian function is used to fit the distribution of FF for each intermediate process and the width of the Gaussian function is taken as the corresponding statistical uncertainty of the FF. The resultant FFs are listed in Table III.

Signal MC samples modeled according to the fit result are generated to compare the projections of the Dalitz plots with data and to calculate the fit bias, which will be discussed in Sec. IV D. The Dalitz plot projections are shown in Fig. 3. To evaluate the goodness of fit with a χ^2/NDF criterion, we calculate $\chi^2 = \sum \left(\frac{N_{\rm data} - N_{\rm MC}}{\sigma_{\rm data}}\right)^2$ of the fit using an adaptive binning of the Dalitz plot of $m^2(K^+K^-)$ versus $m^2(K^-\pi^+)$, in which each bin has at least 10 events. Here $N_{\rm data}$, $\sigma_{\rm data}$ and $N_{\rm MC}$ refer to the

TABLE III. The results on the magnitudes, phases, FFs and significances for the six amplitudes. The first and second uncertainties are the statistical and systematic, respectively.

Amplitude	Magnitude (ρ)	Phase (ϕ)	FFs (%)	Significance (σ)
$D_s^+ \to \bar{K}^*(892)^0 K^+$	1.0 (fixed)	0.0 (fixed)	48.3±0.9±0.6	> 20
$D_s^+ \to \phi(1020)\pi^+$	1.09±0.02±0.01	6.22±0.07±0.04	40.5±0.7±0.9	> 20
$D_s^+ \to S(980)\pi^+$	2.88±0.14±0.17	4.77±0.07±0.07	19.3±1.7±2.0	> 20
$D_s^+ \to \bar{K}_0^*(1430)^0 K^+$	1.26±0.14±0.16	2.91±0.20±0.23	3.0±0.6±0.5	8.6
$D_s^+ \to f_0(1710)\pi^+$	0.79±0.08±0.14	1.02±0.12±0.06	1.9±0.4±0.6	9.2
$D_s^+ \to f_0(1370)\pi^+$	0.58±0.08±0.08	0.59±0.17±0.46	1.2±0.4±0.2	6.4

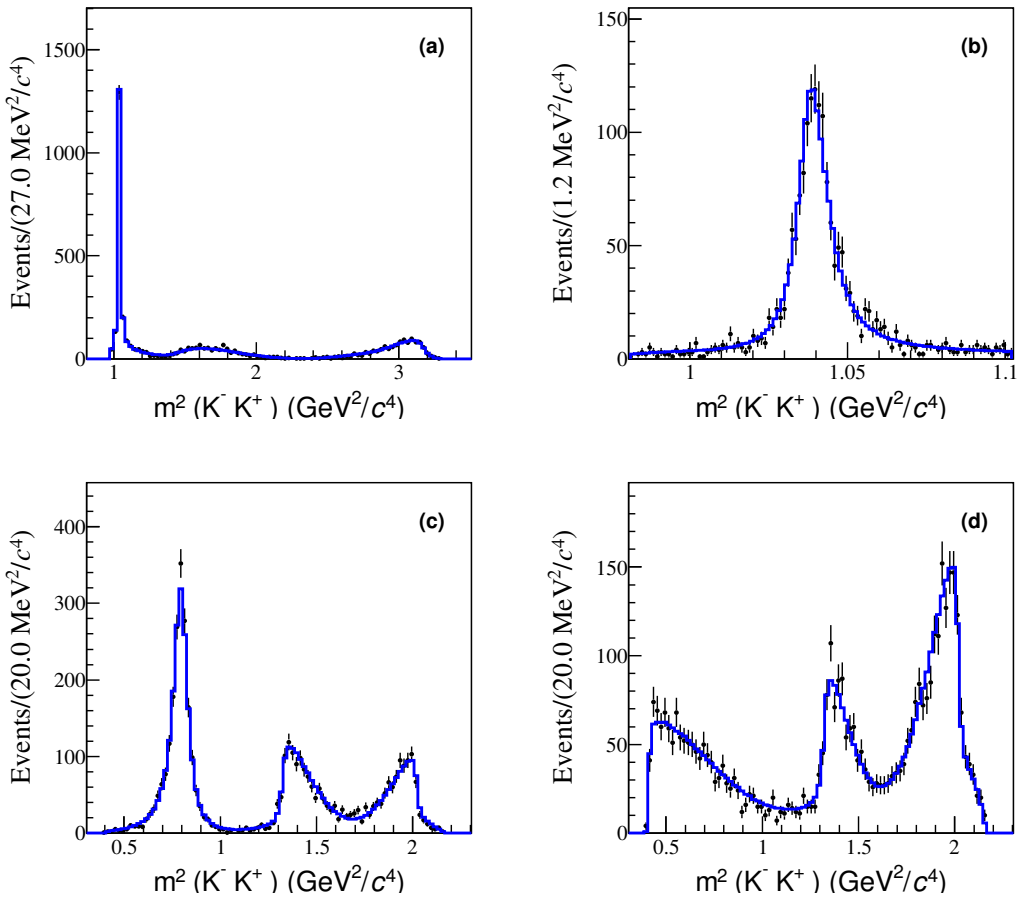

FIG. 3. Dalitz plot projections (a) $m^2(K^+K^-)$, (b) $m^2(K^+K^-)$ near the $\phi(1020)$ peak, (c) $m^2(K^-\pi^+)$ and (d) $m^2(K^+\pi^+)$ from the nominal fit. The data are represented by points with error bars and the solid lines indicate the signal MC sample.

number of data events, the error of $N_{\rm data}$ and the number of signal MC events in each bin, respectively. We find a $\chi^2/{\rm NDF} = 290.0/280$.

D. Systematic Uncertainty

The following categories of systematic uncertainties are studied for the amplitude analysis:

I Resonance parameters. The masses and widths of resonances are shifted by their corresponding uncertainties. For the $S(980)$, m_0 and Γ_0 are shifted

according to the errors from Eq. (A8) in Appendix A. The mass and width of $f_0(1370)$ are shifted according to the uncertainties from Ref. [18]. The parameters of $\bar{K}_0^*(1430)^0$ are shifted according to the errors from Ref. [19]. For other states, uncertainties are taken from the PDG [7].

II The effective radius in the Blatt-Weisskopf barrier factor is varied within the range $[1.0, 5.0]$ GeV^{-1} for intermediate resonances and $[3.0, 7.0]$ GeV^{-1} for D_s mesons.

III Fit bias. Pull distribution checks using 300 signal MC samples are performed to obtain the fit bias. Here the pull value for a certain parameter x is defined as $(x_{\rm true} - x_{\rm MC})/\sigma_{x_{\rm MC}}$, where $x_{\rm MC}$ and $\sigma_{x_{\rm MC}}$ are the value and the statistical error of x obtained from the fit to a certain signal MC sample and $x_{\rm true}$ refers to the true value of x used in the MC generation. The signal MC samples each have the same size as the data. A Gaussian function is used to fit the pull distribution. The quadrature sum of the mean value and the error of mean in the pull distribution fit is taken as the corresponding systematic uncertainty in units of the corresponding statistical error.

IV Detector effects. These effects are related to the efficiency difference between MC simulation and data caused by PID and tracking, reflected in the γ_ϵ in Eq. (9). The PID efficiencies are studied using clean samples of $e^+e^- \to K^+K^-K^+K^-$, $K^+K^-\pi^+\pi^-$, $K^+K^-\pi^+\pi^-\pi^0$, $\pi^+\pi^-\pi^+\pi^-$ and $\pi^+\pi^-\pi^+\pi^-\pi^0$, while a clean sample of $e^+e^- \to K^+K^-\pi^+\pi^-$ is used for the study of tracking efficiencies. These efficiencies are also used in the BF measurement (Sec. V C) and MIPWA (Sec. A). The uncertainties associated with γ_ϵ are obtained by performing alternative amplitude analyses varying PID and tracking efficiencies according to their uncertainties.

V Model assumptions. We replace the Flatté expression in Eq. (14) with the LASS model [20]. For the $S(980)$, Eq. (A6) is replaced with the Flatté parameterization [21] to describe the lineshape of the $S(980)$ and the parameters in the Flatté parameterization are obtained from the fit to $|S|^2$ in Fig. 9(a). The quadrature sum of the shifts in the results are taken as the corresponding systematic uncertainties.

VI Background estimation. We subtract the contribution of the background by assigning a negative weight to the background events in the likelihood calculation [22]. The shifts of parameters are taken as the systematic uncertainties related to background estimation.

VII Contributions with statistical significances less than 5σ. The intermediate processes with statistical significances less than 5σ are added in the nominal fit one by one. The quadrature sum of each parameter variations is taken as the corresponding systematic uncertainty.

Systematic uncertainties on the magnitudes, phases and FFs are summarized in Table IV and the total uncertainties are obtained as the sum of all the contributions in quadrature.

V. BRANCHING FRACTION MEASUREMENT

A. Efficiency and Data Yields

After the selection described in Sec. III, the tag technique is also used to perform the BF measurement. We use the same eight tag modes as in Sec. IV. For each tag mode, if there are multiple tag D_s candidates in an event, the candidate with $M_{\rm rec}$ closest to the nominal mass of D_s^* [7] is retained. The ST yields are obtained by the fits to the D_s invariant mass distributions, as shown in Fig. 4, along with the mass windows listed in Table II. The signal shape is modeled as the MC-simulated shape convolved with a Gaussian function, while background is parameterized as a second-order Chebychev polynomial. Fits to $m_{\rm tag}$ for inclusive MC are performed to estimate the corresponding ST efficiencies. The ST yields ($Y_{\rm ST}$) and ST efficiencies ($\epsilon_{\rm ST}$) are listed in Table V.

After the best candidates of ST D_s^- mesons are identified, we search for the $D_s^+ \to K^+K^-\pi^+$. Only one DT D_s^+ candidate with the average mass of tag D_s^- and signal D_s^+ closest to the nominal mass of D_s is retained for each tag mode in an event. The DT efficiencies, listed in Table VI, are obtained based on the signal MC samples.

As $D_s^- \to K^+K^-\pi^-$ is not only the signal mode but also one of the tag modes, we divide the events into two categories:

- Cat. A: Tag D_s^- decays to one of the tag modes except $D_s^- \to K^+K^-\pi^-$. The inclusive MC sample with the signal removed shows no peaking background around the fit range of $1.90 < m_{\rm sig} < 2.03$ GeV/c^2. Thus, the DT yield is determined by the fit to $m_{\rm sig}$, shown in Fig. 5(a). The background is described with a second-order Chebychev polynomial. The DT yield is 3497 ± 64.

- Cat. B: Tag D_s^- decays to $K^+K^-\pi^-$. As both of the two D_s mesons decay to the signal modes, we fit dM (the mass of the signal D_s^+ minus that of the tag D_s^-), which is shown in Fig. 5(b). Here, the background is described by a second-order Chebychev polynomial. The DT yield is 1651 ± 42.

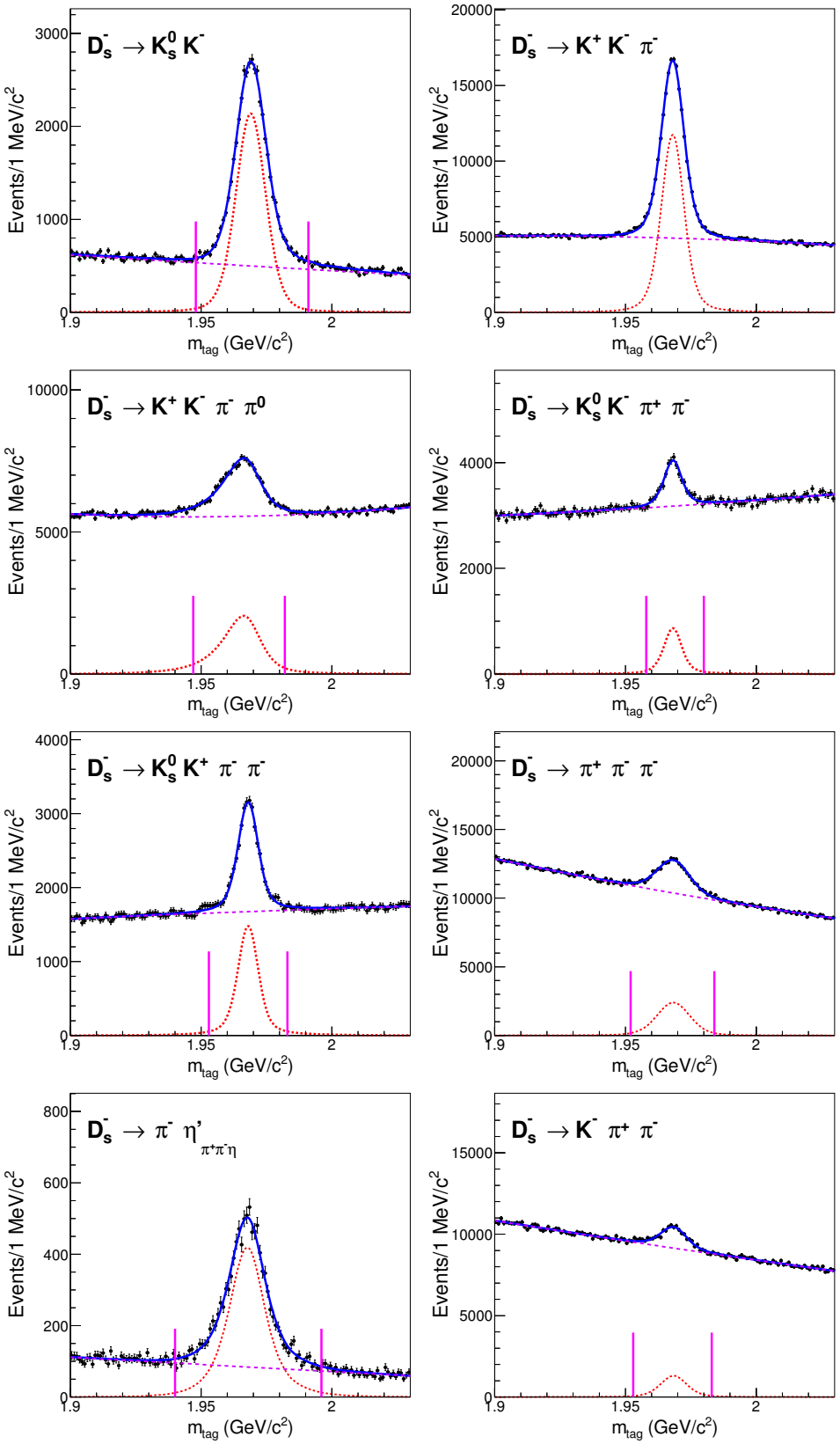

FIG. 4. Fits to the $m_{\rm tag}$ distributions of data. The points with error bars indicate data and the solid lines indicate the fit. Red short-dashed lines are signal, violet long-dashed lines are background. The region within the purple lines denotes the signal region.

TABLE IV. Systematic uncertainties on the ϕ, ρ and FFs for different amplitudes in units of the corresponding statistical uncertainties. Here I, II, III, IV, V, VI and VII denote the propagator parameterizations of the resonances, the effective radius of Blatt-Weisskopf barrier factor, fit bias, detector effects, model assumptions, background estimation and contributions with statistical significances less than 5σ, respectively. The quadrature sums of these terms are taken as the total systematic uncertainties.

Amplitude	Source							
	I	II	III	IV	V	VI	VII	Total
$D_s^+ \to \bar{K}^*(892)^0 K^+$	FF	0.32	0.29	0.14	0.41	0.14	0.10	0.14	0.65
$D_s^+ \to \phi(1020)\pi^+$	ϕ	0.49	0.10	0.06	0.07	0.08	0.02	0.04	0.52
	ρ	0.49	0.14	0.08	0.41	0.19	0.01	0.17	0.71
	FF	0.44	1.13	0.04	0.40	0.08	0.01	0.15	1.29
$D_s^+ \to S(980)\pi^+$	ϕ	0.98	0.25	0.04	0.11	0.06	0.03	0.15	1.03
	ρ	1.11	0.17	0.09	0.11	0.20	0.17	0.23	1.18
	FF	1.16	0.15	0.04	0.09	0.05	0.04	0.25	1.20
$D_s^+ \to \bar{K}_0^*(1430)^0 K^+$	ϕ	1.02	0.48	0.05	0.21	0.09	0.06	0.16	1.16
	ρ	1.00	0.36	0.15	0.20	0.19	0.02	0.21	1.12
	FF	0.76	0.35	0.11	0.22	0.19	0.03	0.20	0.92
$D_s^+ \to f_0(1710)\pi^+$	ϕ	0.31	0.25	0.04	0.14	0.17	0.01	0.17	0.49
	ρ	1.17	1.23	0.09	0.11	0.11	0.11	0.01	1.71
	FF	0.71	1.21	0.04	0.16	0.10	0.10	0.01	1.42
$D_s^+ \to f_0(1370)\pi^+$	ϕ	2.66	0.27	0.12	0.09	0.28	0.21	0.20	2.71
	ρ	1.01	0.32	0.21	0.09	0.05	0.03	0.21	1.10
	FF	0.42	0.30	0.15	0.06	0.15	0.09	0.19	0.60

TABLE V. The ST yields ($Y_{\rm ST}$) and ST efficiencies ($\epsilon_{\rm ST}$). The BFs of the sub-particle (K_S^0, π^0, η and η') decays are not included in the efficiencies.

Tag mode	Mass window (GeV/c^2)	$Y_{\rm ST}$	$\epsilon_{\rm ST}(\%)$
$D_s^- \to K_S^0 K^-$	[1.948, 1.991]	31987± 314	47.66±0.07
$D_s^- \to K^+K^-\pi^-$	-	141189± 643	40.90±0.03
$D_s^- \to K^+K^-\pi^-\pi^0_{\gamma\gamma}$	[1.947, 1.982]	37899±1739	10.36±0.03
$D_s^- \to K_S^0 K^-\pi^+\pi^-$	[1.958, 1.980]	7999± 236	18.67±0.12
$D_s^- \to K_S^0 K^+\pi^-\pi^-$	[1.953, 1.983]	15723± 290	21.51±0.06
$D_s^- \to \pi^-\pi^-\pi^+$	[1.952, 1.984]	38157± 873	50.05±0.15
$D_s^- \to \pi^-\eta'_{\pi^+\pi^-\eta_{\gamma\gamma}}$	[1.940, 1.996]	8009± 142	19.43±0.06
$D_s^- \to K^-\pi^+\pi^-$	[1.953, 1.983]	17112± 561	45.66±0.22

B. Tagging Technique and Branching Fraction

For the DT samples with a certain tag mode α, we have

$$Y_{\rm ST}^{\alpha} = 2N_{D_s^+D_s^-}\mathcal{B}_{\rm tag}^{\alpha}\epsilon_{\rm tag}^{\alpha}, \tag{19}$$

and

$$\begin{array}{ll} N_{\rm sig}^{{\rm obsA},\alpha} = 2N_{D_s^+D_s^-}\mathcal{B}_{\rm tag}^{\alpha}\mathcal{B}_{\rm sig}\epsilon_{\rm tag,sig}^{\alpha}, & \text{for Cat. A} \\ N_{\rm sig}^{{\rm obsB},\alpha} = N_{D_s^+D_s^-}\mathcal{B}_{\rm tag}^{\alpha}\mathcal{B}_{\rm sig}\epsilon_{\rm tag,sig}^{\alpha}, & \text{for Cat. B} \end{array} \tag{20}$$

where $N_{D_s^+D_s^-}$ is the total number of $D_s^{*\pm}D_s^{\mp}$ produced from e^+e^- collision; the yields $N_{\rm sig}^{{\rm obsA},\alpha}$ and $N_{\rm sig}^{{\rm obsB},\alpha}$ refer to the yields with tag mode α for Cat. A and Cat. B, respectively; $\mathcal{B}_{\rm tag}$ and $\mathcal{B}_{\rm sig}$ are the BFs of a specific tag mode and the signal mode, respectively; $\epsilon_{\rm tag}$ is the efficiency to reconstruct the tag mode; $\epsilon_{\rm tag,sig}$ is the efficiency to reconstruct both the tag and signal decay modes.

Using the above equations, one can obtain:

$$\mathcal{B}_{\rm sig} = \frac{N_{\rm sig}^{\rm obsA} + 2N_{\rm sig}^{\rm obsB}}{\sum_{\alpha} Y_{\rm ST}^{\alpha}\epsilon_{\rm tag,sig}^{\alpha}/\epsilon_{\rm tag}^{\alpha}}, \tag{21}$$

where the yields $N_{\rm sig}^{\rm obsA}$, $N_{\rm sig}^{\rm obsB}$ and $Y_{\rm ST}^{\alpha}$ are obtained from data, while $\epsilon_{\rm tag}$ and $\epsilon_{\rm tag,sig}$ can be obtained from the updated inclusive MC samples. The process $D_s^+ \to K^+K^-\pi^+$ in the updated inclusive MC is generated with the Dalitz model obtained in Sec. IV.

TABLE VI. The DT efficiencies ($\epsilon_{\rm DT}$).The BFs of the subparticle (K^0_S, π^0, η and η') decays are not included in the efficiencies.

Tag mode	$\epsilon_{\rm DT}(\%)$
$D_s^- \to K^0_S K^-$	18.59±0.14
$D_s^- \to K^+K^-\pi^-$	17.41±0.06
$D_s^- \to K^+K^-\pi^-\pi^0$	4.33±0.03
$D_s^- \to K^0_S K^-\pi^+\pi^-$	8.03±0.11
$D_s^- \to K^0_S K^+\pi^-\pi^-$	8.25±0.09
$D_s^- \to \pi^-\pi^-\pi^+$	20.84±0.13
$D_s^- \to \pi^-\eta'_{\pi^+\pi^-\eta_{\gamma\gamma}}$	8.30±0.11
$D_s^- \to K^-\pi^+\pi^-$	19.07±0.13

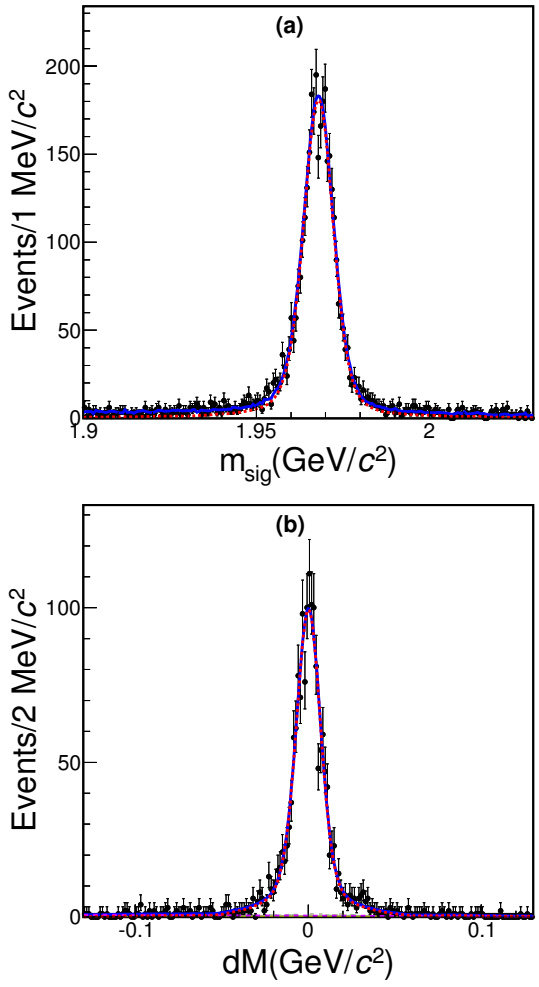

FIG. 5. Fit of $m_{\rm sig}$ for (a) Cat. A and dM for (b) Cat. B. The signal shapes are the corresponding simulated shapes convolved with a Gaussian function and the background shapes are described with second-order Chebychev polynomials.

C. Systematic Uncertainty

The following sources are taken in account to calculate systematic uncertainty in the BF.

- Uncertainty in the number of ST D_s^- candidates. We perform alternative fits with different background shapes and signal shapes to obtain these uncertainties. We change the background shape from a second-order Chebychev polynomial to a third-order Chebychev polynomial and the relative change of BF is 0.18%. The systematic uncertainty in signal shape is determined to be 0.16% by performing an alternative fit without convolution with the Gaussian smearing function. The quadrature sum of these terms, that is the uncertainty in the number of ST D_s^- candidates, is 0.23%.

- DT signal shape. The systematic uncertainty due to the signal shape is studied with the fit without the Gaussian function convolved, the DT yield shift is taken as the related uncertainty.

- DT background shape. For background shape in the fit, a third-order Chebychev polynomial is used to replace the nominal one. The quadrature sum of the BF shifts is taken as the related uncertainty.

- Fit bias. The updated inclusive MC samples are used as fake data to estimate the possible fit bias. The BF for each sample is determined and the relative difference between the average of BFs and the MC truth value is 0.1%, which is negligible.

- $K^\pm$ and $\pi^\pm$ tracking/PID efficiency. The ratios between data and MC efficiencies are weighted by the corresponding momentum spectra of signal MC events. We obtain the systematic uncertainties related to tracking efficiency to be 0.5% for each kaon track and 0.2% for each pion track based on the study of the tracking efficiency. The systematic uncertainties related to PID efficiencies are estimated to be 0.5% for each $K^\pm$ and 0.4% for each $\pi^\pm$. Tracking efficiency systematics are added linearly for the three tracks, as are the PID efficiency systematics.

- MC statistics. The uncertainty due to the MC statistics is obtained as $\sqrt{\sum_\alpha f_\alpha(\frac{\delta_{\epsilon_\alpha}}{\epsilon_\alpha})^2}$, where f_α is the DT yield fraction, ϵ_α is the DT signal efficiency of the tag mode α and δ_{ϵ_α} is the error on ϵ_α due to the limited MC statistics.

- Dalitz model. The uncertainty from the Dalitz model is estimated as the change of efficiency when the Dalitz model parameters (c_n) are varied according to the error matrix.

All of the systematic uncertainties mentioned above are summarized in Table VII. We take the quadrature sum of the systematic uncertainties above as the total systematic uncertainty in the BF of $D_s^+ \to K^+K^-\pi^+$.

TABLE VII. The relative systematic uncertainties on the BF. The quadrature sum of all contributions is taken as the total uncertainty.

Source	Sys. Uncertainty (%)
Number of D_s^-	0.2
Signal shape	0.5
Background shape	0.9
Fit bias	0.1
$K^\pm$ and $\pi^\pm$ Tracking efficiency	1.2
$K^\pm$ and $\pi^\pm$ PID efficiency	1.4
MC statistics	0.6
Dalitz model	0.5
Total	2.3

VI. CONCLUSION

This paper presents the amplitude analysis of the decay $D_s^+ \to K^+K^-\pi^+$. The results on FFs for $D_s^+ \to f_0(1370)\pi^+$, $D_s^+ \to f_0(1710)\pi^+$ and $D_s^+ \to f_0(980)\pi^+/a_0(980)\pi^+$ are consistent with those of BaBar and E687. In addition, our results on FFs also agree with those of CLEO, except for $D_s^+ \to f_0(980)\pi^+/a_0(980)\pi^+$ and $D_s^+ \to f_0(1370)\pi^+$ where 2.4σ and 3.4σ differences, respectively, with CLEO are observed.

In this analysis, as $a_0(980)$ and $f_0(980)$ overlap and parameters of $a_0(980)$ and $f_0(980)$ are not well measured, we have extracted the S-wave lineshape in the low end of K^+K^- mass spectrum with a model-independent method, as shown in Appendix A.

We have also measured the BF $\mathcal{B}(D_s^+ \to K^+K^-\pi^+) = (5.47 \pm 0.08_{\rm stat} \pm 0.13_{\rm sys})\%$ which is currently the most precisise measurement. Comparisons with other results are presented in Tables VIII and IX.

TABLE VIII. Comparisons of BFs among CLEO collaboration, Belle collaboration, BaBar collaboration and this analysis.

$\mathcal{B}\ (D_s^+ \to K^+K^-\pi^+)(\%)$	Collaboration
$5.55 \pm 0.14_{\rm stat} \pm 0.13_{\rm sys}$	CLEO [23]
$5.06 \pm 0.15_{\rm stat} \pm 0.21_{\rm sys}$	Belle [24]
$5.78 \pm 0.20_{\rm stat} \pm 0.30_{\rm sys}$	BaBar [25]
$5.47 \pm 0.08_{\rm stat} \pm 0.13_{\rm sys}$	BESIII(this analysis)

With $\mathcal{B}(\bar{K}^*(892)^0 \to K^-\pi^+)$ and $\mathcal{B}(\phi(1020) \to K^+K^-)$ from PDG [7], we obtain $\mathcal{B}(D_s^+ \to \bar{K}^*(892)^0K^+) = (3.94 \pm 0.12)\%$ and $\mathcal{B}(D_s^+ \to \phi(1020)\pi^+) = (4.60 \pm 0.17)\%$, which are consistent with corresponding theory predictions [1].

ACKNOWLEDGMENTS

The BESIII collaboration thanks the staff of BEPCII and the IHEP computing center for their strong support. This work is supported in part by National Key Basic Research Program of China under Contract No. 2015CB856700; National Natural Science Foundation of China (NSFC) under Contracts Nos. 11625523, 11635010, 11735014, 11822506, 11835012, 11935015, 11935016, 11935018, 11961141012; the Chinese Academy of Sciences (CAS) Large-Scale Scientific Facility Program; Joint Large-Scale Scientific Facility Funds of the NSFC and CAS under Contracts Nos. U1732263, U1832207; CAS Key Research Program of Frontier Sciences under Contracts Nos. QYZDJ-SSW-SLH003, QYZDJ-SSW-SLH040; 100 Talents Program of CAS; INPAC and Shanghai Key Laboratory for Particle Physics and Cosmology; ERC under Contract No. 758462; German Research Foundation DFG under Contracts Nos. 443159800, Collaborative Research Center CRC 1044, FOR 2359, FOR 2359, GRK 214; Istituto Nazionale di Fisica Nucleare, Italy; Ministry of Development of Turkey under Contract No. DPT2006K-120470; National Science and Technology fund; Olle Engkvist Foundation under Contract No. 200-0605; STFC (United Kingdom); The Knut and Alice Wallenberg Foundation (Sweden) under Contract No. 2016.0157; The Royal Society, UK under Contracts Nos. DH140054, DH160214; The Swedish Research Council; U. S. Department of Energy under Contracts Nos. DE-FG02-05ER41374, DE-SC-0012069

Appendix A: Model-independent Partial Wave Analysis in the Low K^+K^- Mass Region

A MIPWA is performed to determine the S-wave lineshape near the threshold of K^+K^- mass spectrum. As we need higher statistics in this MIPWA, the event selection in this section is different from those in the main part of the paper.

In the data sample used in the MIPWA, $D_s^+ \to K^+K^-\pi^+$ candidates are reconstructed according to the selections in Sec. III. The daughter tracks are further subjected to a 1C kinematic fit constraining them to the nominal D_s^+ mass from PDG [7]; selection of the best $D_s^+ \to K^+K^-\pi^+$ candidate is based on the smallest χ^2 in cases of multiple candidates. The best photon candidate for the decay $D_s^{*\pm} \to D_s^\pm\gamma$, is obtained via the recoiling mass against the signal D_s and the photon: $M_{\rm oth} =$

TABLE IX. The BFs measured in this analysis and quoted from PDG [7].

Process	BF (%)	
	BESIII(this analysis)	PDG
$D_s^+ \to \bar{K}^*(892)^0 K^+$, $\bar{K}^*(892)^0 \to K^-\pi^+$	$2.64 \pm 0.06_{\rm stat} \pm 0.07_{\rm sys}$	2.58 ± 0.08
$D_s^+ \to \phi(1020)\pi^+$, $\phi(1020) \to K^+K^-$	$2.21 \pm 0.05_{\rm stat} \pm 0.07_{\rm sys}$	2.24 ± 0.08
$D_s^+ \to S(980)\pi^+$, $S(980) \to K^+K^-$	$1.05 \pm 0.04_{\rm stat} \pm 0.06_{\rm sys}$	1.14 ± 0.31
$D_s^+ \to \bar{K}_0^*(1430)^0 K^+$, $\bar{K}_0^*(1430)^0 \to K^-\pi^+$	$0.16 \pm 0.03_{\rm stat} \pm 0.03_{\rm sys}$	0.18 ± 0.04
$D_s^+ \to f_0(1710)\pi^+$,$f_0(1710) \to K^+K^-$	$0.10 \pm 0.02_{\rm stat} \pm 0.03_{\rm sys}$	0.07 ± 0.03
$D_s^+ \to f_0(1370)\pi^+$,$f_0(1370) \to K^+K^-$	$0.07 \pm 0.02_{\rm stat} \pm 0.01_{\rm sys}$	0.07 ± 0.05
$D_s^+ \to K^+K^-\pi^+$ total BF	$5.47 \pm 0.08_{\rm stat} \pm 0.13_{\rm sys}$	5.39 ± 0.15

$\sqrt{\left(E_{\rm CMS} - \sqrt{|\vec{p}_{D_s}|^2 + m_{D_s}^2} - E_\gamma\right)^2 - |\vec{p}_{D_s} + \vec{p}_\gamma|^2}$, where E_γ and $\vec{p}_\gamma$ refer to the energy and momentum of a certain photon candidate in e^+e^- center-of-mass system, respectively. The photon candidate resulting in the $M_{\rm oth}$ closest to the nominal D_s mass is chosen as the best one.

A multi-variate analysis (MVA) method is used to suppress background from the $q\bar{q}$ continuum and other open charm processes. With the gradient boosted decision tree classifier (BDTG) provided by TMVA [26], we train the MVA separately with two sets of variables for the two categories depending on the D_s^+ origin. Two categories of events are selected in an $M_{\rm rec}$ versus ΔM 2D plane, where $\Delta M \equiv M(D_s^+\gamma) - m_{\rm sig}$, $m_{\rm sig}$ is the invariant mass of signal D_s and $M(D_s^+\gamma)$ refers to the invariant mass of D_s^+ and the photon from $D_s^{*+} \to D_s^+\gamma$, as shown in Fig. 6. The events that satisfy $|M_{\rm rec} - 2.112| < 0.02$ GeV/c^2 (the region within the red solid lines in Fig. 6) are denoted as category 1, while the events that satisfy $|M_{\rm rec} - 2.112| > 0.02$ GeV/c^2 and $0.112 < \Delta M < 0.167$ GeV/c^2 (the region within the green dashed lines in Fig. 6) are denoted as category 2.

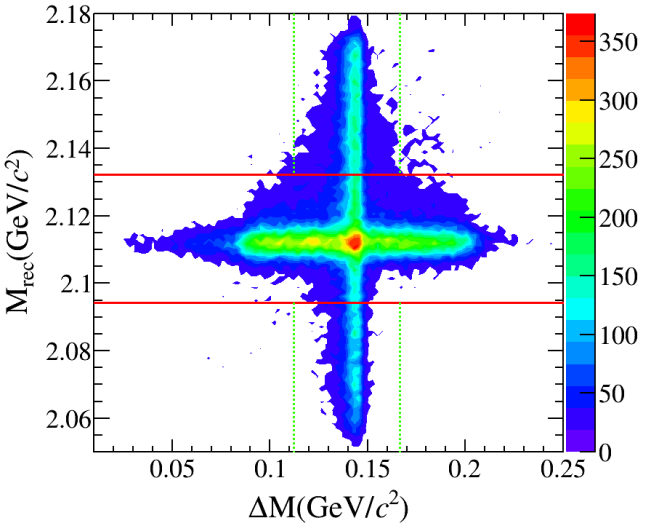

FIG. 6. Two dimensional plane of $M_{\rm rec}$ versus $\Delta M \equiv M(D_s^+\gamma) - m_{\rm sig}$ from the simulated $D_s^+ \to K^+K^-\pi^+$ decays. The red solid (green dashed) lines mark the mass window for the D_s^+ category 1 (category 2) around the $M_{\rm rec}$ (ΔM) peak.

For category 1, the BDTG takes three discriminating variables as input: the recoiling mass $M_{\rm rec}$, the total momentum of the un-reconstructed objects in the event (not part of the $D_s^+ \to K^+K^-\pi^+$ candidate) and the energy of the photon from D_s^*. For category 2, the BDTG takes three additional variables as input: ΔM, $M'_{\rm rec}$ and the total number of charged tracks and neutrals in an event $N_{\rm tracks}$. Here, $M'_{\rm rec}$ is defined as $M'_{\rm rec} = \sqrt{\left(E_{\rm CMS} - \sqrt{p_{D_s\gamma}^2 + m_{D_s^*}^2}\right)^2 - p_{D_s\gamma}^2}$, where $p_{D_s\gamma}$ is the momentum of the $D_s\gamma$ combination in e^+e^- center-of-mass system and $m_{D_s^*}$ is the nominal D_s^* mass. According to studies with the inclusive MC sample, the BDTG requirement gives a relatively pure sample (background less than 4%) and the background ratios of category 1 and category 2 are similar. After applying the BDTG requirement, we fit to the candidate signal D_s invariant mass for both category 1 and category 2 events. The signal shape is modeled with the MC-simulated shape convolved with a double Gaussian function to account for the difference between data and MC simulation, while the background is described with a second-order Chebychev polynomial. This fit gives a background yield in signal region ($1.950 < m_{\rm sig} < 1.986$ GeV/c^2) of 766 ± 30 and a corresponding signal yield of 18600 ± 141, as shown in Fig. 7.

Assuming N is the number of events for a given mass interval of $m(K^+K^-)$, the angular distribution $\frac{dN}{d\cos\Theta}$ can be expanded in terms of spherical harmonic functions:

$$\frac{dN}{d\cos\Theta} = 2\pi \sum_{k=0}^{L_{\rm max}} \langle Y_k^0 \rangle Y_k^0(\cos\Theta), \qquad \text{(A1)}$$

where $L_{\rm max} = 2\ell_{\rm max}$, and $\ell_{\rm max}$ is the maximum orbital angular momentum quantum number required to

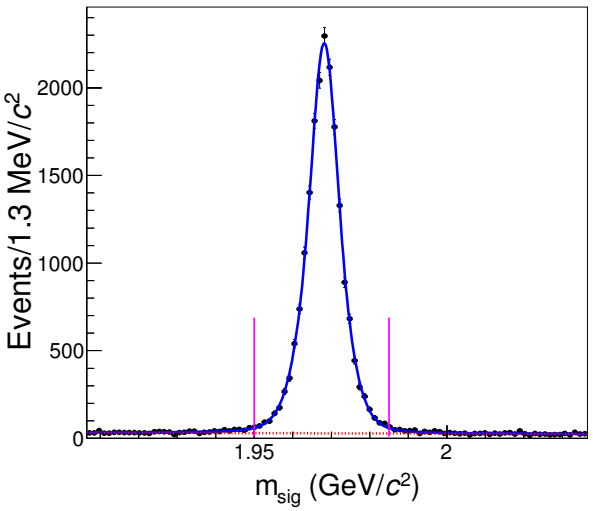

FIG. 7. The fit to the signal D_s invariant mass m_{sig} (the dots with error bars) after BDTG requirement. The area between the pink lines is the signal area of the sample for MIPWA. Here, m_{sig} is the mass without 1C kinematic fit correction. The signal shape is the MC-simulated shape convolved with a double Gaussian function and the background shape (red dotted line) is second-order Chebychev polynomial.

describe the K^+K^- system at $m(K^+K^-)$ (e.g. $\ell_{\max}$ =1 when only S-, P-wave are considered), Θ is the angle between the K^+ direction in the K^+K^- rest frame and the prior direction of the K^+K^- system in the D_s^+ rest frame, $Y_k^0(\cos\Theta) = \sqrt{(2k+1)/4\pi}P_k(\cos\Theta)$ are harmonic functions, $P_k(\cos\Theta)$ is k-th order Legendre polynomial.

The background contribution is subtracted from the selected sample using the shape of the $m(K^-\pi^+)$ versus $m(K^+K^-)$ distribution from the inclusive MC sample, while the background normalization is fixed according to the fit results (see Fig. 7). After that the distribution $dN/d\cos\Theta$ of data are corrected for efficiency and phase space. The distribution $m(K^-\pi^+)$ versus $m(K^+K^-)$ of PHSP MC is used to calculate the efficiency. The correction for the Lorentz invariant phase space factor is calculated as $\rho_{KK} = \sqrt{1-4m_K^2/m^2(K^+K^-)}$, where m_K is the nominal mass of $K^\pm$ [7]. The harmonic functions $Y_k^0(\cos\Theta)$ are normalized as follows:

$$\int_{-1}^{1} Y_k^0(\cos\Theta)Y_j^0(\cos\Theta)d\cos\Theta = \frac{\delta_{kj}}{2\pi}. \tag{A2}$$

Considering the orthogonality condition, we can obtain the expansion coefficients according to Eqs. (A1) and (A2):

$$\left\langle Y_k^0 \right\rangle = \int_{-1}^{1} Y_k^0(\cos\Theta)\frac{dN}{d\cos\Theta}d\cos\Theta. \tag{A3}$$

In this section, the formalism $\sum_{n=1}^{N} Y_k^0(\cos\Theta_n)$ is used to calculate the integral, where Θ_n refers to the Θ of the n-th event.

According to $\left\langle Y_k^0 \right\rangle = \sum_{n=1}^{N} Y_k^0(\cos\Theta_n)$, one obtains the distribution of $\left\langle Y_k^0 \right\rangle$ for k = 0, 1 and 2 at the low end of K^+K^- mass spectrum ($0.988 < m(K^+K^-) < 1.15$ GeV/c^2), as shown in Fig. 8.

Assuming that only S- and P-wave amplitudes are necessary at the low end of K^+K^- mass spectrum, the distribution $dN/d\cos\Theta$ can also be written in terms of the partial wave amplitudes:

$$\frac{dN}{d\cos\Theta} = 2\pi\left|\mathrm{S}Y_0^0(\cos\Theta) + \mathrm{P}Y_1^0(\cos\Theta)\right|^2, \tag{A4}$$

where S and P refer to the amplitudes of S-wave and P-wave, respectively. Comparing Eqs. (A1) and (A4) [27], we can obtain

$$\begin{aligned} |\mathrm{S}|^2 &= \sqrt{4\pi}\left\langle Y_0^0 \right\rangle - \sqrt{5\pi}\left\langle Y_2^0 \right\rangle, \\ \cos\phi_{\mathrm{SP}} &= \frac{\left\langle Y_1^0 \right\rangle}{\sqrt{(2\left\langle Y_0^0 \right\rangle - \sqrt{5}\left\langle Y_2^0 \right\rangle)\sqrt{5}\left\langle Y_2^0 \right\rangle}}, \\ |\mathrm{P}|^2 &= \sqrt{5\pi}\left\langle Y_2^0 \right\rangle, \end{aligned} \tag{A5}$$

where $\phi_{\mathrm{SP}} = \phi_{\mathrm{S}} - \phi_{\mathrm{P}}$ is the phase difference between S-wave and P-wave, ϕ_{S} and ϕ_{P} are the phases of S-wave and P-wave, respectively. Calculating $|\mathrm{S}|^2$, ϕ_{SP} and $|\mathrm{P}|^2$ in every mass interval of $m(K^+K^-)$ in the threshold region, the distribution of $|\mathrm{S}|^2$, $|\mathrm{P}|^2$, ϕ_{SP} and ϕ_{S} can be obtained, as shown in Fig. 9. There are two curves in Fig. 9(c) because of the sign ambiguity of ϕ_{SP} extracted from $\cos\phi_{\mathrm{SP}}$.

We found that the Flatté parameterization [21] is insensitive to the $\pi\pi$ or $\pi\eta$ coupling or the coupling induced between them while fitting the distribution of $|\mathrm{S}|^2$. Therefore, the lineshape of $S(980)$ is empirically parameterized with the following formula:

$$A_{S(980)} = \frac{1}{m_0^2 - m^2 - im_0\Gamma_0\rho_{KK}}. \tag{A6}$$

Fitting the distribution of $|\mathrm{S}|^2$ in Fig. 9(a) with $|A_{S(980)}|^2$, we can obtain the values of m_0 and Γ_0:

$$\begin{aligned} m_0 &= (0.919 \pm 0.006_{\mathrm{stat}})\ \mathrm{GeV}/c^2, \\ \Gamma_0 &= (0.272 \pm 0.040_{\mathrm{stat}})\ \mathrm{GeV}. \end{aligned} \tag{A7}$$

Figure 9(a) shows the fit result. The χ^2/NDF of the fit is 44.46/38 = 1.17.

The $S(980)$ mass central value obtained from the fit is much lower than the threshold of $m(K^+K^-)$ (about 0.988 GeV/c^2). Therefore the distribution of ϕ_{S} is expected to be roughly constant. The phase ϕ_{P} of the $\phi(1020)$ is given by Eq. (12) in Sec. 6; it increases rapidly

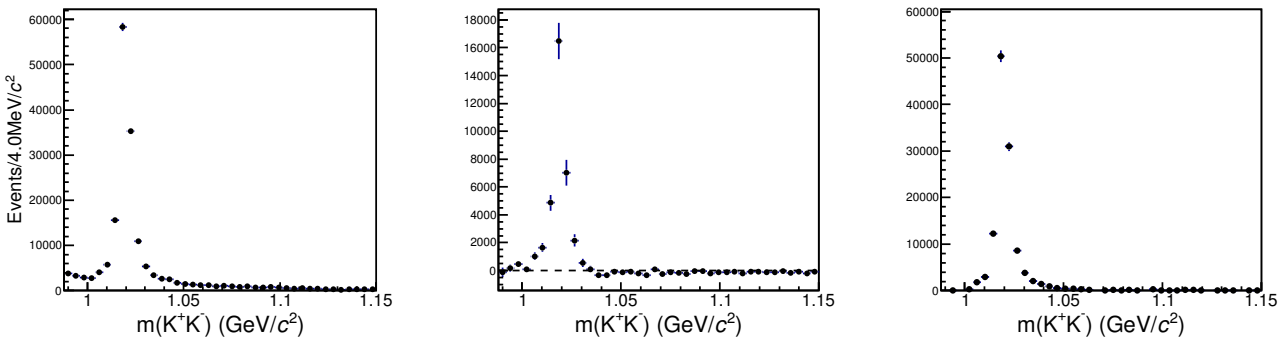

FIG. 8. The distribution of (a) $\langle Y_0^0 \rangle$, (b) $\langle Y_1^0 \rangle$ and (c) $\langle Y_2^0 \rangle$ in K^+K^- threshold region.

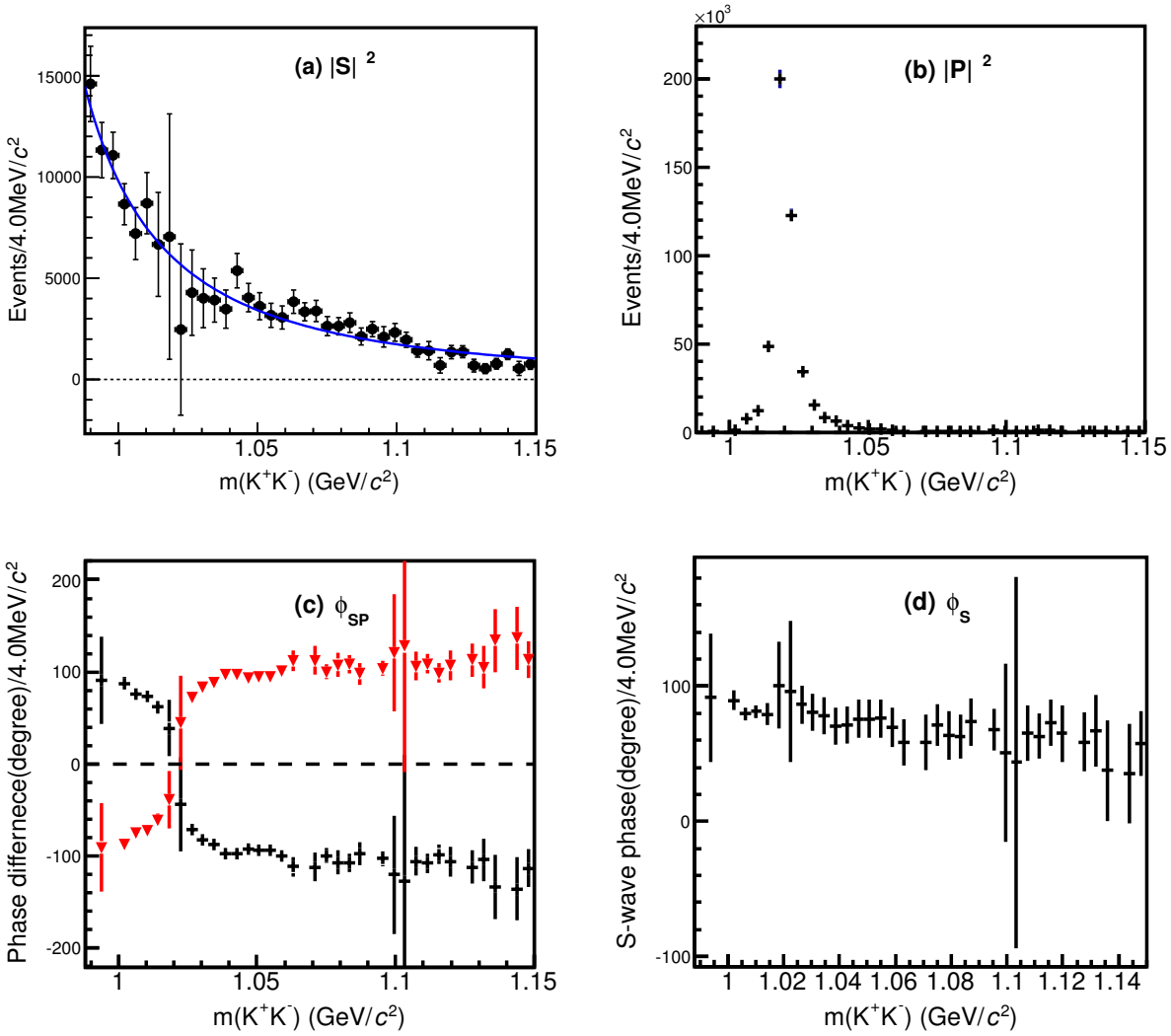

FIG. 9. The distribution of (a) $|S|^2$, (b) $|P|^2$, (c) ϕ_{SP} and (d) ϕ_S in the threshold region of $m(K^+K^-)$. The description of the fit in (a) can be found in the following text.

near the $\phi(1020)$ peak because of its narrow width. Then the sign ambiguity of $\phi_{\rm SP}$ is solved by choosing the black curve in Fig. 9(c), which decreases rapidly near the mass of the $\phi(1020)$, ensuring that $\phi_{\rm S} = \phi_{\rm P} + \phi_{\rm SP}$ is roughly constant. The resulting phase of the $S(980)$, $\phi_{\rm S}$, is shown in Fig. 9(d).The values of $|{\rm S}|^2$ (arbitrary units), $|{\rm P}|^2$ (arbitrary units) and $\phi_{\rm S}$ in every mass interval of the threshold region are listed in Table X.

Systematic uncertainties considered for the MIPWA include:

- Data-MC agreement for the BDTG output. A control sample is obtained with same event selection as that in Sec. IV A due to its high purity, but without the kinematic fit criteria. The efficiency of data and MC samples from the BDTG requirement is then considered, where the efficiency of data (MC) is defined as $e_{\rm data} = \frac{N_{d1}}{N_{d0}}$ ($e_{\rm MC} = \frac{N_{M1}}{N_{M0}}$), where N_{d0} (N_{M0}) and N_{d1} (N_{M1}) are the number of events before and after applying the BDTG requirement. We can now correct the data sample with $\frac{e_{\rm data}}{e_{\rm MC}}$. We fit the corrected shape of the $S(980)$ and take the shift of m_0 and Γ_0 as the systematic uncertainty.

- Background subtraction. We change the bin size, fit range and replace the background shape with a third-order Chebychev polynomial in the fit shown in Fig. 7. New fits are performed and we take the quadrature sum of the shifts as the uncertainty of the background fraction. Then we vary the background fraction, (3.9 ± 0.3)%, within its uncertainty and take the shift of the $S(980)$ fit results as the systematic uncertainty related to the background fraction. The background shape of inclusive MC sample is also replaced with that of sideband ($1.90 < m_{\rm sig} < 1.95$ GeV/c^2 and $1.986 < m_{\rm sig} < 2.03$ GeV/c^2) for data to perform a fit and the shift is taken as the systematic uncertainty related to the background shape. The quadrature sum of the shifts of m_0 and Γ_0 are 0.002 GeV/c^2 and 0.001 GeV, respectively.

- Particle identification (PID) and tracking efficiency difference between data and MC simulation. To estimate the detector effects related to the difference of PID and tracking efficiency between data and MC simulation, we weight each event with the data/MC efficiency differences and fit the shape of the $S(980)$. The shift of m_0 and Γ_0 are 0.001 GeV/c^2 and 0.013 GeV, respectively.

- The $f_0(1370)$ contribution. The $f_0(1370)$ contribution in the $S(980)$ region was subtracted according to the measured FF. The shape of $f_0(1370)$ at the low end of $m_{K^+K^-}$ mass spectrum was obtained from the MC simulation. The interference effect was ignored. The resulting shifts of m_0 and Γ_0 are 0.001 GeV/c^2 and 0.003 GeV, respectively.

- Fit range. We vary the fit range from [0.988, 1.15] GeV/c^2 to [0.988, 1.145] GeV/c^2, which results in m_0 and Γ_0 shifts of 0.002 GeV/c^2 and 0.003 GeV, respectively.

All of the systematic uncertainties mentioned above are summarized in Table XI. The quadrature sum of the uncertainties is taken as the total uncertainty. We obtain the result for m_0 and Γ_0 with statistical and systematic errors to be:

$$\begin{aligned} m_0 &= (0.919 \pm 0.006_{\rm stat} \pm 0.030_{\rm sys})\ {\rm GeV}/c^2, \\ \Gamma_0 &= (0.272 \pm 0.040_{\rm stat} \pm 0.024_{\rm sys})\ {\rm GeV}, \end{aligned} \tag{A8}$$

which are consistent with the BaBar analysis [4]. Note that m_0 and Γ_0 in Eq. (A8) are only used for the parameterization of the $S(980)$ in Sec. IV.

TABLE X. The values of $|S|^2$ (arbitrary units), $|P|^2$ (arbitrary units) and ϕ_S; the units chosen preserve the relative $|S|^2$ and $|P|^2$ sizes. Uncertainties in the table are statistical only. Some values of ϕ_S are not listed in the table because the values of $\langle Y_2^0 \rangle$ in the corresponding mass intervals are negative and a physical solution for ϕ_{SP} cannot be found according to Eq. (A5).

$m(K^+K^-)$ (GeV/c^2)	$\|S\|^2$ (arbitrary units)	$\|P\|^2$ (arbitrary units)	ϕ_S (degrees)
[0.988, 0.992]	14593±1860	−1137±1401	-
[0.992, 0.996]	11326±1364	168±1027	92± 48
[0.996, 1.000]	11064±1143	−531± 850	-
[1.000, 1.004]	8659±1015	1006± 748	90± 7
[1.004, 1.008]	7207±1281	7292±1003	80± 5
[1.008, 1.012]	8703±1509	11746±1200	81± 5
[1.012, 1.016]	6669±2565	48763±2066	79± 8
[1.016, 1.020]	7051±6057	199740±5048	101± 32
[1.020, 1.024]	2466±4232	122645±3520	96± 52
[1.024, 1.028]	4292±2108	34363±1748	87± 14
[1.028, 1.033]	4009±1455	15046±1212	81± 13
[1.033, 1.037]	3922±1088	8108± 887	78± 14
[1.037, 1.041]	3480± 944	5945± 768	70± 14
[1.041, 1.045]	5376± 854	3707± 678	71± 14
[1.045, 1.049]	4043± 696	2103± 551	76± 14
[1.049, 1.053]	3621± 665	1858± 530	76± 14
[1.053, 1.057]	3167± 599	1680± 467	76± 14
[1.057, 1.061]	3063± 569	1333± 448	70± 15
[1.061, 1.065]	3841± 582	685± 461	59± 17
[1.065, 1.069]	3343± 439	−45± 324	-
[1.069, 1.073]	3377± 525	395± 413	59± 21
[1.073, 1.077]	2635± 474	684± 368	71± 15
[1.077, 1.081]	2632± 426	357± 320	64± 18
[1.081, 1.085]	2802± 485	647± 377	63± 16
[1.085, 1.089]	2121± 421	287± 332	74± 18
[1.089, 1.093]	2487± 369	−185± 278	-
[1.093, 1.097]	2105± 505	1041± 409	68± 15
[1.097, 1.101]	2326± 440	100± 355	51± 66
[1.101, 1.105]	1962± 369	47± 286	44±137
[1.105, 1.109]	1422± 323	216± 246	65± 21
[1.109, 1.114]	1420± 453	777± 377	63± 17
[1.114, 1.118]	697± 377	903± 307	73± 17
[1.118, 1.122]	1351± 330	234± 257	65± 21
[1.122, 1.126]	1373± 297	−60± 229	-
[1.126, 1.130]	690± 312	340± 255	59± 22
[1.130, 1.134]	535± 246	130± 197	67± 27
[1.134, 1.138]	772± 261	205± 199	38± 37
[1.138, 1.142]	1246± 266	−71± 200	-
[1.142, 1.146]	545± 350	456± 298	35± 37
[1.146, 1.150]	763± 262	206± 205	58± 24

TABLE XI. Systematic uncertainties of the partial wave analysis in the low K^+K^- mass region. The quadrature sum of all contributions is taken as the total uncertainty.

Source	m_0 (GeV/c^2)	Γ_0 (GeV)
BDTG	0.030	0.020
Background subtraction	0.002	0.001
PID and Tracking	0.001	0.013
$f_0(1370)$	0.001	0.003
Fit range	0.002	0.003
Total	0.030	0.024

[1] H. Y. Cheng, C. W. Chiang and A. L. Kuo, Phys. Rev. D **93**, 114010 (2016).

[2] P. L. Frabetti *et al.* (E687 Collaboration), Phys. Lett. B **351**, 591 (1995).

[3] R. E. Mitchell *et al.* (CLEO Collaboration), Phys. Rev. D **79**, 072008 (2009).

[4] P. del Amo Sanchez *et al.* (BABAR Collaboration), Phys. Rev. D **83**, 052001 (2011).

[5] M. Ablikim *et al.* (BESIII Collaboration), Phys. Rev. Lett. **123**, 112001 (2019).

[6] D. Cronin-Hennessy *et al.* (CLEO Collaboration), Phys. Rev. D **80**, 072001 (2009).

[7] P.A. Zyla *et al.* (Particle Data Group), Prog. Theor. Exp. Phys. **2020**, 083C01 (2020).

[8] R. M. Baltrusaitis *et al.* (Mark III Collaboration), Phys. Rev. Lett. **56**, 2140 (1986).

[9] M. Ablikim *et al.* (BESIII Collaboration), Nucl. Instrum. Meth. A **614**, 345 (2010).

[10] C. Zhang for BEPC & BEPCII Teams, Performance of the BEPC and the progress of the BEPCII, in: Proceeding of APAC, 2004, pp. 15-19, Gyeongju, Korea.

[11] S. Agostinelli *et al.* (GEANT4 Collaboration), Nucl. Instrum. Meth. A **506**, 250 (2003).

[12] R. G. Ping, Chin. Phys. C **38**, 083001 (2014).

[13] S. Jadach, B. F. L. Ward and Z. Was, Phys. Rev. D **63**, 113009 (2001).

[14] D. J. Lange, Nucl. Instrum. Meth. A **462**, 152 (2001); R. G. Ping, Chin. Phys. C **32**, 599 (2008).

[15] J. C. Chen, G. S. Huang, X. R. Qi, D. H. Zhang and Y. S. Zhu, Phys. Rev. D **62**, 034003 (2000); R. L. Yang, R. G. Ping and H. Chen, Chin. Phys. Lett. **31**, 061301 (2014).

[16] E. Richter-Was, Phys. Rev. D **62**, 034003 (2000).

[17] B. S. Zou and D. V. Bugg, Eur. Phys. J. A **16**, 537 (2003).

[18] M. Alblikim *et al.* (BES Collaboration), Phys. Lett. B **607**, 243 (2005).

[19] G. Bonvicini *et al.* (CLEO Collaboration), Phys. Rev. D **78**, 052001 (2008).

[20] M. Alblikim *et al.* (BESIII Collaboration), Phys. Rev. D **95**, 072001 (2017).

[21] S. M. Flatté *et al.*, Phys. Lett. **38B**, 232 (1972).

[22] M. Alblikim *et al.* (BESIII Collaboration), Phys. Rev. D **95**, 072010 (2017).

[23] P. U. E. Onyisi *et al.* (CLEO Collaboration), Phys. Rev. D **88**, 032009 (2013).

[24] A. Zupanc *et al.* (BELLE Collaboration), JHEP **1309**, 139 (2013).

[25] P. del Amo Sanchez *et al.* (BABAR Collaboration), Phys. Rev. D **82**, 091003 (2010).

[26] A. Hoecker *et al.*, TMVA - Toolkit for Multivariable Data Analysis, PoS ACAT, (2007), arXiv:physics/0783039.

[27] S. U. Chung, Phys. Rev. D **56**, 7299 (1997).